JOURNAL OF AEROSPACE TECHNOLOGY AND MANAGEMENT

Journal of Aerospace Technology and Management

Aims and Scope

The Journal of Aerospace Technology and Management (JATM) is an open-access journal devoted to research and management on different aspects of aerospace technologies.

For all accepted manuscripts, the correspondence author will be asked to contribute with the Article Processing Charge, which will be applied to editorial services that support the publishing process, like editing, proofreading, indexing and dissemination.

The value is fixed per article, independent of its length and is R$ 800,00 (in Brazilian reais) or U$300,00 (in American dollars). In exceptional cases, the editorial board may waive a contribution upon reasonable request.

JATM accepts manuscripts already published in preprint, considered reliable by the editorial committee, and must be informed in the Open Science Compliance Form that must be submitted as a supplementary file to the Manuscript.

Journal of Aerospace Technology and Management

Journal of Aerospace Technology and Management

(Volume No. 15,   Issue No. 2, May - August 2023)

Contents

Development of a Two-Stroke Cycle Engine for Use in the Agricultural Aviation Sector

Samara Herrmann1,* , Macklini Dalla Nora1 , Thompson Diordinis Metzka Lanzanova

Universidade Federal de Santa Maria – Grupo de Pesquisa em Motores, Combustíveis e Emissões – Santa Maria/RS, Brazil.
2.Directorate General of Education – Kufa/Najaf – Iraq.

A B S T R A C T

Reciprocating internal combustion engines have wide application in agricultural, recreational and experimental aircraft, resulting from their low cost and less complex maintenance compared to other engines. Thus, this work analyzed the performance of a conventional four-stroke engine operating in the two-stroke cycle by means of direct fuel injection and mechanical air supercharging. The use of a supercharger was essential in this design to provide adequate gas exchange inside the cylinder during the long valve overlap required, while direct fuel injection made it possible to reduce the short circuit of air-fuel mixture to the exhaust. Due to the double ignition frequency compared to a four-stroke engine, it was possible to obtain a large power density (40 kW/L) at a speed of 2400 rpm, also a specific fuel consumption of 270 g/kWh with gasoline and 400 g/kWh with ethanol. The use of ethanol in replacement of gasoline made it possible to operate at full load (160 Nm/L) at 800 rpm without the occurrence of knocking combustion.

Keywords: Internal combustion engine; Two-stroke cycle; Agricultural aviation.

I. INTRODUCTION

The agribusiness sector has great importance to Brazilian economy, representing 23.5% of its gross domestic product (GDP) in 2017, as stated by the Brazilian Agriculture and Livestock Confederation (Reuters 2017). Changes in traditional cultivation processes, as introduction of fertilizers and pesticides, have become necessary because of the growth of agricultural production. Mhereb and Norder (2018) affirm that agricultural aviation is an essential component in the process of modernizing Brazilian agriculture and emphasize its great operational capacity. In this sense, agricultural aviation plays a key role in expanding productivity. If compared to land application, it allows the spraying of agrochemicals in a larger area in a shorter time. It also provides no contact with soil avoiding its compaction and damage to other crops; besides, it enables the application even in wet soil after heavy rainfall periods (Santos 2005).

According to data from the National Syndicate of Agricultural Aviation Companies (Parceria Agro 2019), at the beginning of 2019 the fleet of agricultural aircraft in Brazil was 2194 units, the state with the largest fleet being Mato Grosso, representing 22.5% of the total, followed by Rio Grande do Sul with

19.5%, and São Paulo with 14.5%. In addition, Brazil has the second largest agricultural aviation fleet in the world, only behind the United States of America, which has about 3600 agricultural aircrafts (NAAA 2019).

The Brazilian agricultural aircraft fleet is mainly composed by the model Ipanema produced by Embraer, which represents almost 60% of the total fleet. Ipanema has a Lycoming piston engine originally fueled with aviation gasoline, but it is converted to ethanol at the aircraft manufacturer in Brazil. Nevertheless, most of the engines of agricultural aircrafts operated in Brazil are fueled with aviation gasoline (AvGas). According to Hausen (2011), all aircraft engines operating in Brazil are imported, except for those adapted from automotive engines used in experimental aviation. Imported engines increase the cost of acquisition and maintenance. On the other hand, the adaptation of automotive engines, often performed in an amateur manner, exposes the pilot and areas close to the flight region to safety-related risks. In-flight engine failure was the largest cause of serious incidents between 2008 and 2017, according to Santos et al. (2018).

Internal combustion engines are widely used in general aviation, which includes private aircraft, experimental aircraft and nonscheduled air transport. In such cases, the engine operating in the four-stroke cycle is predominant. Two-stroke internal combustion engines are widely used in ultralight aircraft and gyroplane due its simpler architecture, making them less expensive and lighter.

Homa (2013) emphasizes that two-stroke engines are not extensively used in general airplanes because they present higher fuel consumption and short-circuiting of fuel to the exhaust gases, besides lubrication and durability problems. The last two disadvantages are linked to the fact that the crankcase is used for pumping the air-fuel mixture to the cylinder.

The short circuit of the air-fuel mixture is a typical problem of two-stroke engines. Since intake and exhaust ports are positioned in front of each other in the cylinder and their opening and closing are controlled by the positioning of the piston itself, part of the new air-fuel mixture is not burned and goes directly to the exhaust, increasing the fuel consumption. In this sense, it is advantageous to use direct fuel injection in the combustion chamber, as in diesel cycle engines, so the fuel only enters the combustion chamber after the exhaust port is closed and the scavenging process is carried out with air only, solving the shortcircuiting issue. Zhang et al. (2013) has proposed the use of solenoid valves as in four-stroke engines; also, Leighton et al. (1994) and Duret and Moreau (1990) proposed low-cost injectors with compressed air assistance.

In the matter of component lubrication and durability, Sato et al. (1992), Hundleby (1990) and Nomura and Nakamura (1993) suggest the use of overhead valves and forced oil lubrication on the moving parts, as in four-stroke engines. In that way, there is no need to add lubricant oil to the mixture to achieve relatively adequate lubrication. Also, the durability problems associated with the high temperature gradient in the cylinder due to the presence of intake and exhaust ports are reduced.

With the crankcase being part of the lubrication system, an external compressor is required to pump the intake air into the cylinder, which is usually known as blower. Although the fuel short-circuiting problem is solved by direct injection, there is still the short-circuiting of air; therefore, a significant part of the intake air is directly lost to the exhaust. Hence, more compressor work is required to ensure the air supply, which consequently reduces the engine efficiency.

In relation to the fuel itself, AvGas has the addition of tetraethyllead as an antiknock agent, an extremely harmful component to the environment and toxic if ingested by humans. This additive allows an increase up to 100 in the octane number of AvGas. In this scenario, ethanol appears as a possible solution, once it is a renewable fuel with easier commercial access in Brazil, presenting an octane number around 113. Furthermore, Hausen (2011) stated that operating with ethanol reduces operational costs about US$ 40 per flight hour.

Consequently, it stands out the lack of an aeronautical engine of national origin fueled with a more commercially accessible and less harmful to the environment fuel, which could integrate modern control systems already applied to automotive engines.

Therefore, the present study explores the application of the two-stroke cycle, well known for its high power and torque density, to the modern architecture of four-stroke engines with better fuel consumption and overall durability. Ethanol was evaluated in such prototype engine in parallel to gasoline as a possible renewable substitute for the mostly used fossil fuel, considering its wide availability in Brazil

METHODOLOGY

Engine Specification

The tests were implemented in a research engine of the Centre for Advanced Powertrain and Fuels at Brunel University, London. The engine model was a Ricardo Hydra two/four-stroke Camless, as specified in Table 1.

Table 1. Engine Ricardo Hydra Camless data.

Number of cylinders	1
Swept volume	0.35 dm³
Bore	81.6 mm
Stroke	66.9 mm
Compression ratio	11.8:1
Combustion chamber	Pent roof with four valves and a central spark plug
Fuel injector	Magneti Marelli solenoid type with six orifices
Exhaust port opening	120° CA ATDC
Intake port opening	130° CA ATDC
Exhaust port closing	230° CA ATDC
Intake port closing	240° CA ATDC

Two fuels were used to conduct the experiments: European gasoline with 95 octanes that is close to aviation gasoline with 100 octanes; and anhydrous ethanol (99,9%) with an equivalent number of octanes close to 109. The instant of fuel injection was adjusted for a better compromise between short circuit and quality of combustion, since early injection leads to fuel loss directly to the exhaust and late injections do not provide enough time for homogenization of the mixture. In general, it was varied between 210° and 270° after top dead center (TDC). The ignition timing was adjusted to provide maximum torque without the occurrence of knocking, a phenomenon extremely harmful to the engine since it causes overheating and may lead internal components to failure.

The tests were performed at three specific torque values: 32, 96 and 160 Nm/L. Also, the engine speed was varied between 800 and 2400 rpm in steps of 400 rpm.

The fuel temperature near the injector was maintained at 300 ± 5 K. Fuel pressure near the injector was kept at 14.5 ± 0.5 Mpa.

The supercharger power consumption was calculated considering a 70% total efficiency in the compression process, which is a usual value found for roots-type blowers employed in this field.

All testing points were performed at steady state conditions and 200 consecutive engine cycles were acquired for each point evaluated after stabilizing oil and coolant temperatures.

Engine Instrumentation

The engine assembly diagram and its respective instrumentation is shown in Fig. 1. The sensors and equipment used in the instrumentation are listed below.

• Hasting HMF-200: air mass flow measurement;

• Endress + Houser Promass 83A Coriollis Effect: fuel mass flow measurement;

• Kistler 6061B: piezoelectric sensor for in-cylinder pressure measurement;

• Kistler 4007 BA20F/BA5F: piezoresistive sensor for intake and exhaust pressure measurements;

• Thermocouple type K: admission, exhaust, lubricant oil and fuel line temperature measurements;

• Ricardo rCube Unit: ignition timing, fuel injection and valve parameters control;

• Encoder LeineLinde: incremental encoder for correlation between pressure data and crankshaft angle with 720 pulses per revolution;

• National Instrumental NI US-6353 Board: data acquisition and process in real-time;

• Air compressor AVL 515: air supercharging with close loop control of pressure and temperature.
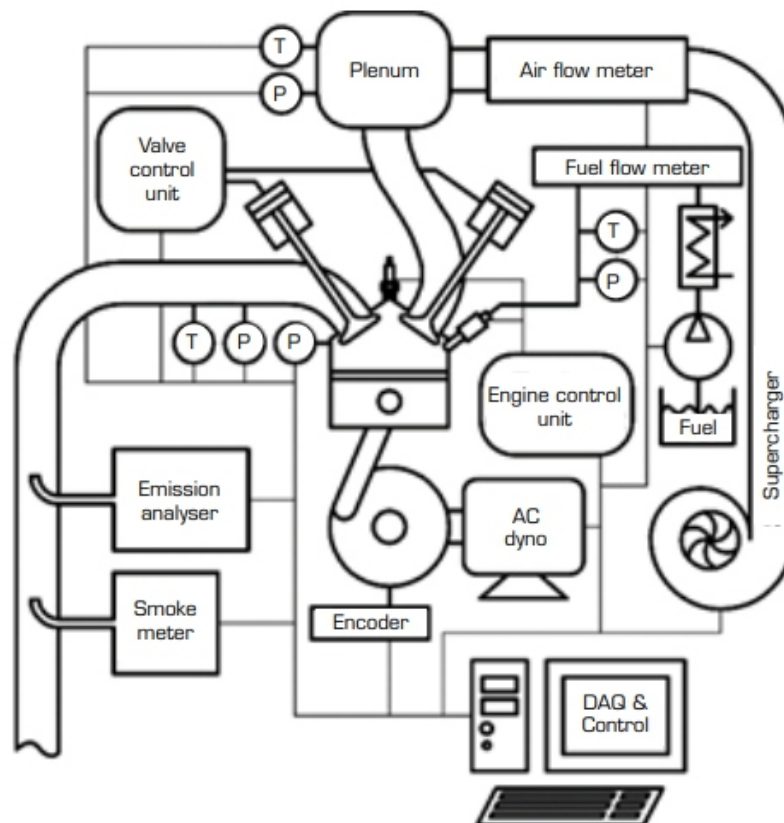
Figure 1. Engine assembly and instrumentation diagram. Source: Dalla Nora et al. (2016).

Figure 2 shows a modification made to the combustion chamber in order to reduce the problem of air short-circuiting. A mask has been added allowing the reduction of fresh air passing directly to the exhaust. More discussion on this combustion chamber feature and other design options are presented by Dalla Nora et al. (2016).
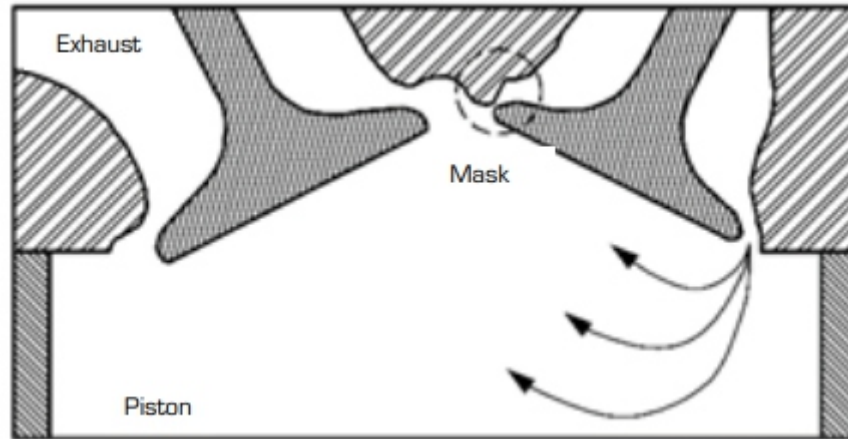
Figure 2. Combustion chamber geometry modification. Source: Dalla Nora et al. (2016).

RESULTS

The results are presented in relation to the engine speed in rpm and its load from low (32 Nm/L) to medium (96 Nm/L) and high load (160 Nm/L). The specific torque in Nm/L unit reflects the expected torque of the motor according to the displaced volume. The graphs on the left show the results for gasoline, while the right shows the results for ethanol.

Figure 3 shows the indicated efficiency for different speeds with the engine fueled by gasoline and ethanol. Such parameter compares the total amount of energy supplied to the engine through the fuel to the expansion work developed inside the cylinder. The supercharger operation was also considered by evaluating the amount of power diverted from the engine to the theoretical boosting device. As expected, all curves have less amplitude when the turbocharger is operated since part of the shaft power is transferred to the compressor. Ethanol operation showed greater efficiencies, around 33% at medium load and in the speed range between 800 and 1200 rpm. Gasoline showed greater efficiency in the same range of operation, with a value of approximately 32%. The lower efficiencies are presented with the higher engine loads since the compressor consumes even more power in this condition. The lower overall efficiency of gasoline was also a result of the retarded ignition timing required to avoid knocking combustion, which was not the case of ethanol operation when the maximum torque was achieved at all times.
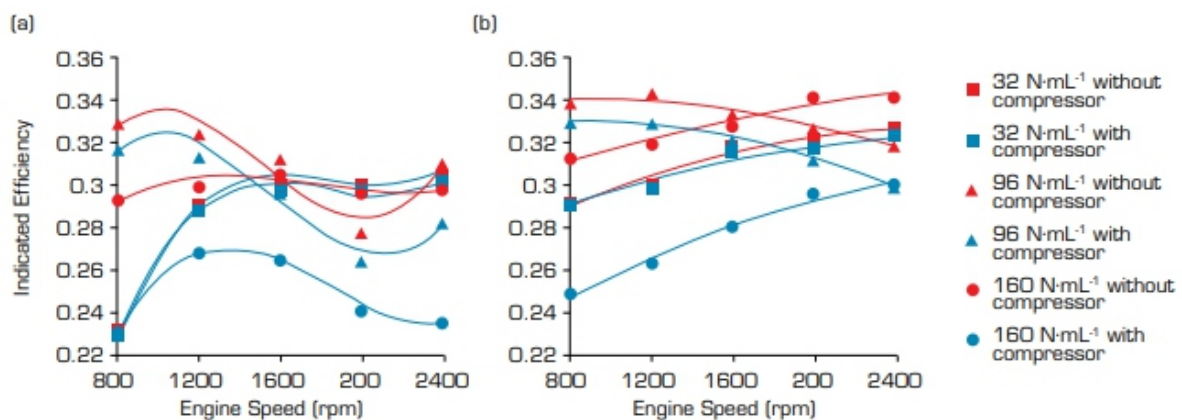
Figure 3. Indicated efficiency for (a) gasoline and (b) ethanol.

That way, Fig. 4 presents the specific fuel consumption (ISFC). The fuel consumption increases when the compressor power requirement is increased, what is associated with efficiency reduction. Gasoline had a lower specific fuel consumption than ethanol, mainly because of the lower heating value of ethanol, approximately 64% of gasoline (27 MJ/kg versus 42 MJ/kg). The different behavior of the 96 Nm/L operation in comparison to the 32 and 160 Nm/L conditions are attributed mainly to combustion efficiency, which is a compromise among fueling and gas-exchanging as presented by Dalla Nora et al. (2018).
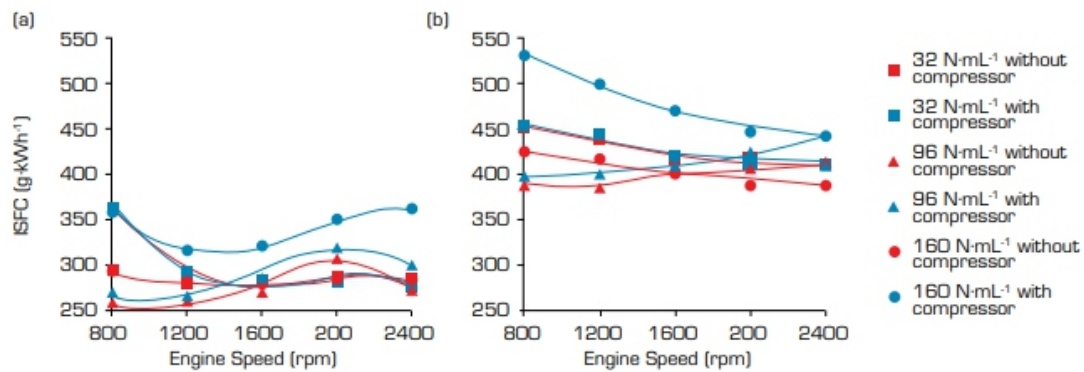
Figure 4. Specific fuel consumption for (a) gasoline and (b) ethanol.

Figure 5 shows the specific power for the different engine speeds and loads tested. The maximum specific power of 40 kW/L was set for both fuels tested. This resulted from a compromise between specific fuel consumption and supercharger power consumption, although higher power output could be obtained at the cost of lower overall engine efficiency. According to Fig. 4, in this condition, the specific fuel consumption of ethanol was just below 400 g/kWh and of gasoline it was around 270 g/kWh.

Taking as an example, the EMB-203 aircraft engine, Lycoming IO-540-K1J5, naturally aspirated and four-stroke cycle. This engine develops a power output of 238 kW at 2700 rpm from a swept volume of 8.874 dm3 and a compression ratio of 8.7:1, resulting in a specific power output of 26 kW/L. The efficiency of this engine is around 28.5% when operating with AvGas (Lycoming 2006). In this context, although both engine models do not require a reduction drive in the propeller connection, the four-stroke operation requires a larger number of cylinders and a larger displacement and consequently a heavier and bulker engine.

The 912 series engine from the manufacturer Rotax, widely used in ultralight, small and experimental aircraft, is a naturally aspirated four-stroke cycle model with four cylinders, swept volume of 1.352 dm3 and compression ratio of 11:1 (Rotax, 2010).

It has a power of 40 kW/L at a speed above 4000 rpm with a specific torque of approximately 90 Nm/L. This model, despite having a smaller swept volume in relation to the previous comparison, indicates the need for a reduction drive since the rotation is too high for direct propeller operation, which adds weight and complexity to the system.
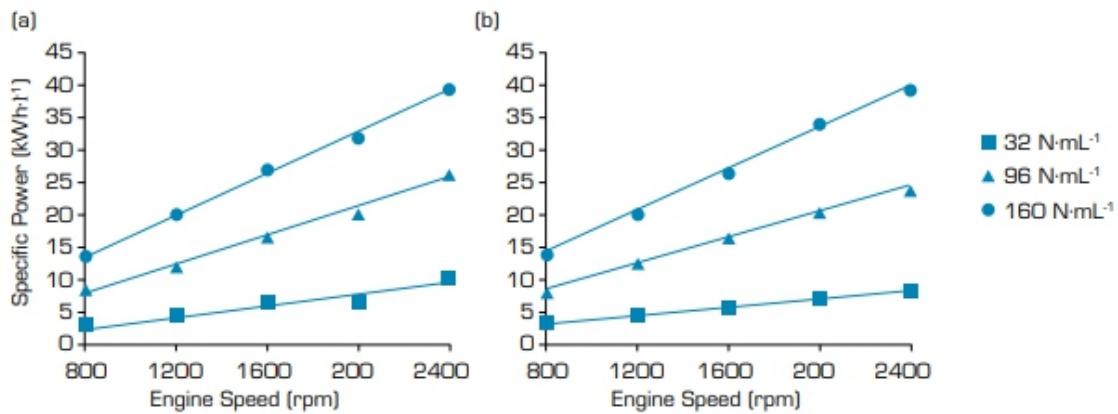
Figure 5. Specific power for (a) gasoline and (b) ethanol.

Figure 6 shows the ignition advance set for each engine speed and load value seeking minimum spark advance for best torque (MBT). It was seen that a greater advance in ignition was achieved for ethanol and the MBT condition was reached for the three load values. For gasoline, the ignition advance was limited by knocking combustion. This is a result of the greater resistance to detonation given by the higher octane number of ethanol (109 RON) compared to European gasoline (95 RON), besides ethanol higher latent heat of vaporization which reduces the in-cylinder temperature at the onset of combustion. The spark timings for gasoline were retarded at higher engine speeds due to the larger amount of hot in-cylinder gas trapped, which induced knock. On the other hand, ethanol demonstrated regular ignition timings despite of two speed conditions at the minimum load tested. This was a result of combustion instabilities as it can be found elsewhere (Dalla Nora et al. 2018).

Figure 7 shows the maximum pressures in the cylinder. The values observed are in the range between 2 and 6 MPa for both fuels. In the case of gasoline, there are significantly lower pressure values above 1600 rpm, what is due to the knocking limitation. This knocking limitation forced a reduction in the ignition advance and, as a result, a peak pressure in the cylinder occurring later in the expansion cycle. In general, ethanol presented lower pressure values for the same load, which can be attributed to its higher cooling capacity, given its higher latent heat of vaporization than gasoline.
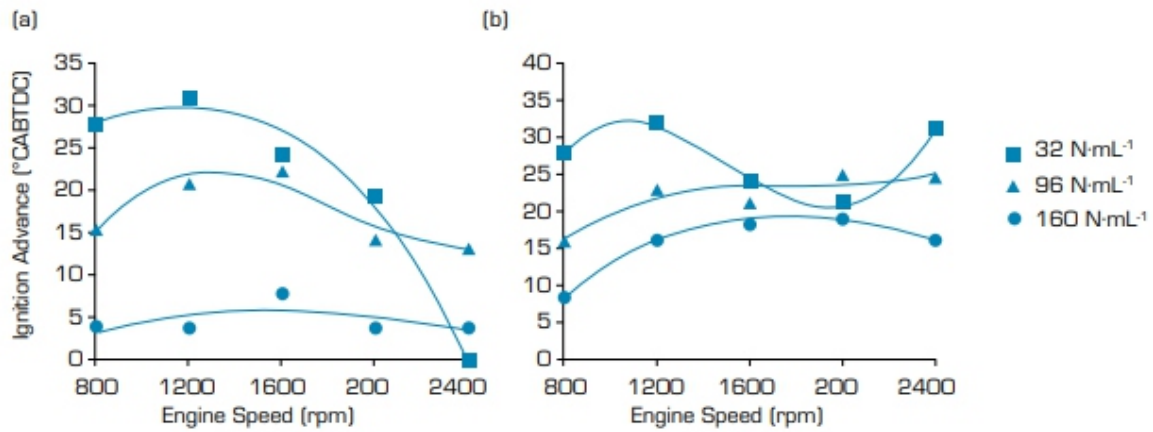
Figure 6. Ignition advance for (a) gasoline and (b) ethanol.
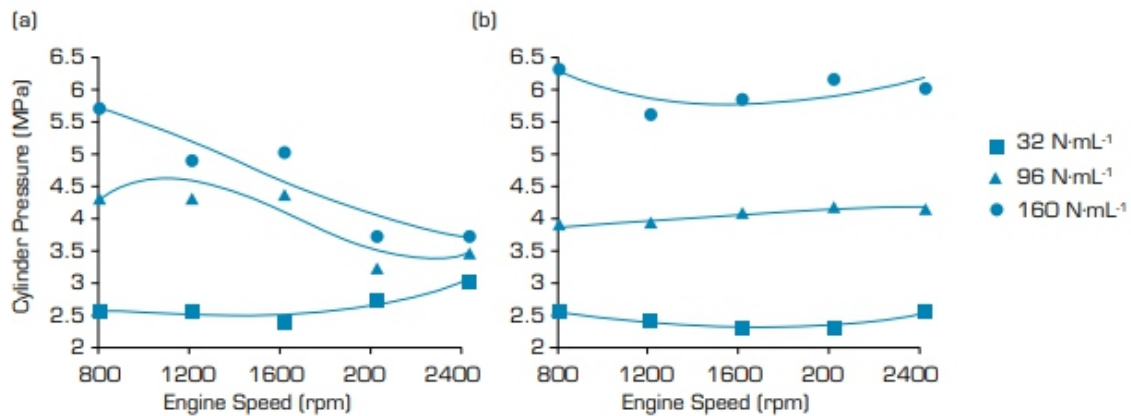
Figure 7. Maximum in-cylinder pressure for (a) gasoline and (b) ethanol.

The maximum pressure values in the cylinder are a significant advantage of the two-stroke cycle operation, since lower cylinder pressures allow to reduce structural stresses and to optimize combustion by ignition advancing around the MBT. In this way, less robust engine can be achieved and, consequently, of lower weight and cost.

Figure 8 shows the inlet pressure values for each engine speed and load. For both gasoline and ethanol fuels, the highest pressures are presented together with the highest speeds and higher loads. The higher the engine speeds, the shorter was the absolute time available for gas exchanging and hence a higher intake pressure was required to displace the burned gases and keep the engine load. The lower values presented by ethanol at high load and high speed are also reflected in the higher indicated efficiency, which may be attributed to its oxygenated content. It should be noted that the observed intake pressure values could be easily achieved with air superchargers available on the market. Intake pressures usually found in the automotive market range from 110 to 250 kPa.

Figure 9 shows the exhaust gas temperature (EGT). The lowest temperature was found at minimum engine speed and maximum load at approximately 460 K, while the highest temperature was achieved at maximum speed and maximum load at approximately 720 K. At lower loads the exhaust temperature is essentially a function of the engine load, while at higher loads the temperature has a significant contribution of the effect of the air short circuiting due to higher intake pressures. It is possible to notice lower temperatures in ethanol operation when compared to gasoline, due to the higher thermal efficiency of the biofuel used.
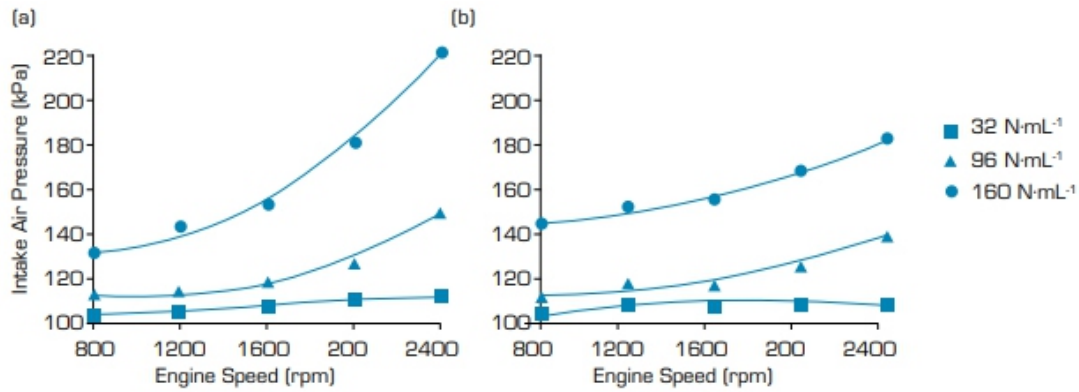
Figure 8. Intake air pressure for (a) gasoline and (b) ethanol.
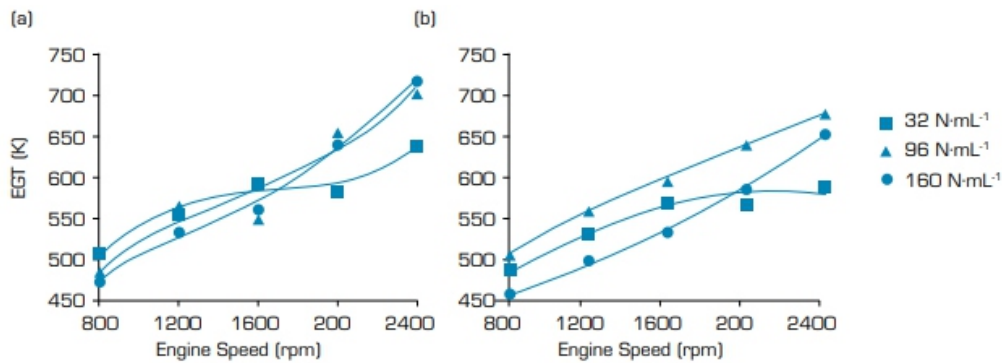
Figure 9. Exhaust gases temperature for (a) gasoline and (b) ethanol.

It is also interesting to observe a competing effect between heat generation rate due to higher engine speed and the air short circuit rate from intake to exhaust. This explains a higher temperature for the medium load of 96 Nm/L, while at the higher load there was a cooling of the exhaust gas and the average temperature was the lowest observed between the loads tested.

The low exhaust temperatures observed, given the cooling effect of the exhaust gases by the portion of short-circuited air may present undesirable effects when turbochargers are applied since the energy available at the exhaust will be lower due to its lower temperature.

CONCLUSIONS

It could be observed that a four-stroke engine operating in the two-stroke cycle can provide superior power density allied with similar overall efficiency, while maintaining the reliability of a four-stroke cycle engine architecture.Ethanol operation shows potential to replace AvGas, reducing the cost of operation and using a fuel from a renewable source without the addition of toxic components.Also, the ethanol operation made it possible to reach the MBT without the occurrence of knocking combustion for maximum specific torque.

The absence of knocking reduces the risk of engine failure in operation, in addition to allow an increase in engine efficiency since combustion occurs closer to the optimal point (MBT). Nevertheless, the lower heating value of ethanol results in higher specific consumption and hence a shorter flying range for the same loaded fuel mass, although the higher efficiency of ethanol operation may overcome part of this problem.

The pressures in the cylinder, both for ethanol and gasoline, resulted in lower values compared to four-stroke cycle engines, allowing a less robust, lower cost and lighter engine.

The exhaust temperature found was lower than that observed in four-stroke engines due to the direct passage of part of the intake air, phenomena known as air short-circuiting.

Finally, the supercharging pressure required for engine operation can be easily reached by the technology present in the market for roots or centrifugal type blowers. However, the exhaust backpressure should receive attention when using turbochargers, since there must always be an intake-exhaust positive pressure ratio for the gas exchange to occur.

AUTHOR'S CONTRIBUTIONS

Conceptualization: Herrmann S; Dalla Nora M; Lanzanova TDM; Data curation: Dalla Nora M; Lanzanova TDM; Formal analysis: Herrmann S; Dalla Nora M; Investigation: Dalla Nora M; Methodology: Dalla Nora M; Lanzanova TDM; Software:
Herrmann S; Resources: Dalla Nora M; Lanzanova TDM; Validation: Dalla Nora M; Lanzanova TDM; Writing - Original Draft Preparation: Herrmann S; Writing - Review & Editing: Herrmann S; Dalla Nora M.

DATA AVAILABILITY STATEMENT

All the datasets were generated and analyzed during the current study.

REFERENCES

[NAAA] National Agricultural Aviation Association (2019) Industry facts. [accessed Jun 30 2019]. https://www.agaviation.org/industryfacts.

Dalla Nora M, Lanzanova TDM, Zhao H (2016) Effects of valve timing, valve lift and exhaust backpressure on performance and gas exchanging of a two-stroke GDI engine with overhead valves. Energy Convers Manag 123:71-83. https://doi.org/10.1016/j.enconman.2016.05.059.

Dalla Nora M, Lanzanova TDM, Zhao (2018) Investigation of performance and combustion characteristics of a four-valve supercharged two-stroke DI engine fueled with gasoline and ethanol. Fuel 227:401-411.

Duret P, Moreau J-F (1990) Reduction of pollutant emissions of the IAPAC two-stroke engine with compressed air assisted fuel injection. Paper presented International Congress and Exposition. SAE Technical Paper Series; Detroit, Michigan, United States. https://doi.org/10.4271/900801

Hausen RB (2011) Sistematização de conhecimento para o projeto de motor a etanol para aeronave agrícola (Master thesis).

Santa Maria: Universidade Federal de Santa Maria. In Portuguese.

Homa JM (2013) Aeronaves e motores. São Paulo: ASA.

Hundleby GE (1990) Development of a poppet-valved two-stroke engine - the flagship concept. Paper presented International Congress and Exposition. SAE Technical Paper Series; Detroit, Michigan, United States. https://doi.org/10.4271/900802.

Leighton S, Cebis M, Southern M, Ahem S (1994) The OCP small engine fuel injection system for future two-stroke marine engines. Paper presented International Off-highway & Powerplant Congress & Exposition. SAE Technical Paper Series; Milwaukee, Wisconsin, United States. https://doi.org/10.4271/941687.

Lycoming (2006) Operator's manual Lycoming: O-540, IO-540 series. Williamsport: Lycoming.

Mhereb GA, Norder LAC (2018) Aviação agrícola no Brasil: contexto e caracterização. Confins 36. https://doi.org/10.4000/confins.13638

Nomura K, Nakamura N (1993) Development of a new two-stroke engine with poppet-valves: Toyota s-2 engine. A new generation of two-stroke engines for the future? (Ed. Duret P.). Paper presented

Reuters (2017) Participação do agronegócio no PIB é a maior em 13 anos, estima CNA. G1: Globo. [accessed Jun 30 2019]. https://g1.globo.com/economia/agronegocios/noticia/participacao-do-agronegocio-no-pib-e-a-maior-em-13-anos-estima-cna.ghtml

Rotax (2010) Operator's Manual Rotax Engine Series 912. Rotax Aircraft Engine.

Santos JMF (2005) Aplicação aérea e terrestre: vantagens e limitações comparativas. Paper presented V Congresso Brasileiro de Algodão. CBA; Salvador, Bahia, Brazil.

Santos LCB, Almeida CA, Carpena L, et al. (2018) Aviação particular - sumário estatístico 2008-2017. Centro de Investigação e Prevenção de Acidentes Aeronáuticos (CENIPA). Brasília, Distrito Federal, Brazil.

Sato K, Ukawa H, Nakano M (1992) A two-stroke cycle gasoline engine with poppet valves in the cylinder head - Part II. Paper presented International Congress and Exposition. SAE Technical Paper Series; Detroit, Michigan, United States. https://doi.org/10.4271/920780

Zhang Y, Zhao H, Ojapah M, Cairns A (2013) CAI combustion of gasoline and its mixture with ethanol in a 2-stroke poppet valve DI gasoline engine. Fuel 109(8):661-668.

Experimental and Analytical Study of the Cold Flow Inside a Ramjet Test Engine

Leonardo César Freitas1,* , Olexiy Shynkarenko1

.Universidade de Brasília – Faculdade do Gama – Departamento de Engenharia Aeroespacial–
Brasília/DF – Brazil.

A B S T R A C T

The work is focused on the performance estimation and control of a cold flow inside a ramjet test engine, which initially operates without combustion, preparing the flow for the main propulsive phase. To achieve this objective, a "connected pipe" test bench was assembled. Flow management was performed using the control valve that allows regulating pressure and air mass flow rate in the engine according to its flight conditions through sensors installed at relevant positions. The proportional, integral and derivative (PID) parameters for the flow control algorithm were studied in order to guarantee the stable operation of the engine and correspondence of the flow parameters to predicted ones by the analytical modeling. Experimental results were validated by the numerical and analytical compressible flow models.

Keywords: Ramjet engines; Test facilities; Optimal control; Cold flow tests; Compressible flow.

I. INTRODUCTION

A ramjet is an airbreathing engine that is characterized by having no compressor and turbine sections, unlike a turbofan engine, used in commercial aircrafts. Flow compression is performed by means of a supersonic diffuser that transforms the kinetic energy of the flow into potential energy, increasing its pressure and temperature. After this process, fuel is mixed with air in the combustion chamber, and this mixture, which constitutes the propellant, is burned (Sutton and Biblarz 2010; Hill and Peterson 1992). Flame holders of various configurations are generally used for the flame stabilization inside the combustion chamber due to high flow-to-flame relative velocity. Finally, the combustion products are accelerated and expanded into the atmosphere.

The ramjet engine is generally used in missiles, but its simplicity increase goes along with a limitation: it cannot produce static thrust and cannot operate from rest (Hill and Peterson 1992). As a consequence, ramjet missiles are often equipped with a booster stage that accelerates a missile to supersonic speed at which the ramjet works efficiently (Fry 2004), it does not have to store onboard oxidizer which would increase its weight, but rather aspirate it. Sarisin (2005) further states that the ramjet has a higher specific

impulse than a rocket engine and potential for greater range. However, its operating altitude is limited as it depends on the air intake.

Like any type of engine, a ramjet must be tested before going into operation. Usually, the first type of test to be done on this engine is the "connected pipe" (CP) test, which aims to evaluate the combustion chamber's structural integrity and efficiency using components that simulate the pressure and temperature conditions to which the engine will be subjected in flight (Sarisin 2005). Studies that are usually done after CP tests are the "semi-free jet test", in which the whole engine is tested and the "free jet test", in which the ramjet-propelled vehicle is tested (Sarisin 2005). The last two studies are more complex and more expensive than the CP test (Sarisin et al. 2006). In addition, the CP test requires a lower mass flow rate than the others (Esirgen 2014).

The main object of the current study is the ramjet test engine. It was developed and built by the Chemical Propulsion Laboratory (CPL) of the University of Brasilia in terms of the research project Design and development of a high-maneuverability supersonic missile with ramjet engine. The experimental testing of this engine includes several stages, one of them is the development of a control program of the air valve in order to achieve various operation modes: i) initial flow control for engine ignition, ii) main flow control during the propulsive phase, iii) flow termination (CPL, 2017). The flow behavior in this system is highly nonlinear due to the compressibility, turbulence, and combustion processes, thus it requires a deep study of control and predictable system operation. Due to these considerations, a CP test bench has been built for experimental testing.

Thus, the main objective of this work is the experimental analysis of the cold flow (without combustion) in the CPL test bench and construction of an analytical flow model in the engine.

METHODOLOGY

To achieve the main objective of the work, a ramjet engine test bench has been set up, a proportional, integral and derivative (PID) control system has been implemented and a cold flow model based on the isentropic compressible flow equations, according to Anderson (2016), has been constructed.

Experimental Setup

Test bench schematics and assembly

The air duct of the test bench shown in Fig. 1 consists of the following components: i) compressed air tank, ii) piping, manual valve, iii) flow control valve, iv) ignition system, v) heater, vi) combustion chamber with a supersonic nozzle.

The system components are assembled using standard ASME B16.5 for flange connections. The system is designed to operate using liquid (propane) or solid fuel (paraffin and polyethylene) for ramjet engines. However, in the current work, cold tests only have been performed and the fuel supply system was not introduced.
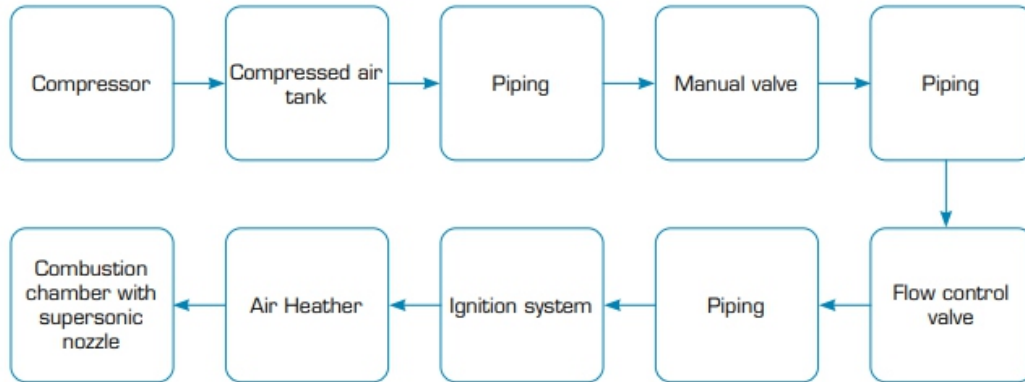
Figure 1. Schematic of the connected pipe test bench.

The compressor supplies the air tank with 5 m3 by a pressure of 10 bar. Such volume of the tank allows executing the flow tests up to 40 s. According to Esirgen (2014), a tank capacity should be high for long tests, and the final tank pressure should be higher than a ramjet combustion chamber pressure in order to compensate losses in the flow path. The maximum allowable tank pressure is 16 bar, which could be achieved by injecting additional air-oxygen mixture from the high-pressure tanks for the oxidizer utilization in the air heater. Pressure and temperature sensors have been installed inside the tank for the stagnation properties measurement during the test. The condensed water has been drained through solenoid valves installed in the air tank and compressor.

The following parts have been installed between the air storage tank and the manual ball valve: i) a "knee", which directs the flow downwards, ii) a straight upright tube, iii) a second knee, which directs the airflow in a horizontal direction, iv) a straight horizontal tube. An S-shaped tube has been installed between the manual valve and the control valve in the horizontal plane. A pressure sensor has been installed near the end of this tube to measure the pressure prior to the control valve. A straight horizontal pipe with a pressure sensor was installed after the control valve. A flexible pipe connects the air supply system with the engine to mitigate the propagation of vibrations from the engine rear to the air supply system (Inman 2014).

Stainless steel AISI 304L was used for the air pipes (cold flow ducts) and AISI 310S for hot flow ducts: the combustion chamber, fuel injection system, ignition system, nozzle support, etc. Such materials have high corrosion resistance due to their capability to form the chromium oxide (Cr_2O_3) protective layer on the surface of pipes (Mouritz 2012).

Flow Control Valve

The airflow control valve aims to regulate the flow properties on the inlet of the ramjet engine (a diffuser), reducing the pressure according to the test program (Sarisin 2005). The valve assembly used in this project consists of three main components: a mechanical globe valve, an electropneumatic linear positioner, which receives an analog electrical signal and converts it into pressure variation, and a spring-diaphragm-type pneumatic actuator, which receives pressurized air of 2.5 bar from the positioner and converts it in motion to a stem responsible for the degree of opening of the valve. The actuator can assume various discrete positions between "fully closed" and "fully open" (EAS 2017, p. 24). According to the valve specifications, its maximum mass flow rate is 2 kg/s. Because of its large size, the mechanical and pneumatic characteristic times of the valve are quite large, the complete valve opening or closing lasts from 4 to 7 s. A big valve response time adds an additional complexity to the building of an efficient algorithm of the valve control program.

Sensors

Two types of sensors have been used in this project and installed at different positions on the test bench (Table 1). Pressure sensors Danfoss MBS-1700 were used for the estimation and control of the flow pressure in the feeding lines and inside the tank. The pressure was acquired with 200 Hz frequency. The active pressure sensor requires 9–32 V DC supply voltage, providing 4–20 mA output with a response time that is less than 4 ms (Danfoss 2016).

Table 1. Sensors installed for the cold flow tests.

ID	Sensor type	Position
P1		Tank
P2		Before control valve
P3	Pressure: Danfoss BS-1700	After control valve
P4		Air heater
P5		Combustion chamber
T1		Tank
T2	Temperature: Omega KQXL-18U-12, KQXL-18U-6	Before air heater
T3		After air heater
T4		Nozzle

The thermocouples used in the project are Omega KQXL-18U-12 and KQXL-18U-6. They are working on the Seebeck Effect producing a voltage between the ends of a heat conductor due to the temperature differential. The typical response time for such thermocouple is close to 0.55 s (Omega Engineering 2019). Not all sensors presented in Table 1 were used in the current study nor have direct relation to this work. They are going to be explored in further publications and are kept to show consistency with future studies.

Fuel Line and Igniter

The cold flow tests were performed in the current work, therefore the fuel line and the ignition system (Shynkarenko et al. 2019b) had been sealed and are not in operation. Fuel inlet lines and the igniter interfaces were closed with caps to prevent the backflow and leakage of the air. The assembly of the air duct containing igniter and fuel supply lines is shown in Fig. 2.
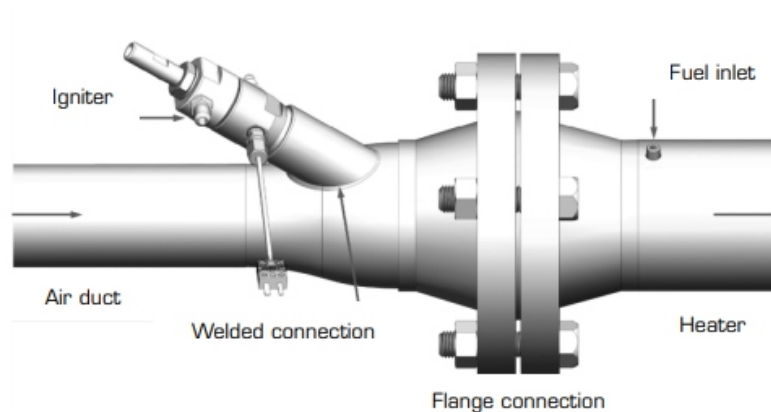
Figure 2. Subassembly of the test stand: air duct, heater, and igniter.

Flow Heater

The airflow heater aims to create the vitiated flow conditions (pressure, mass flow rate, and temperature) equivalent to flow properties at the diffuser exit of a flying ramjet. Its main purpose is to increase the air temperature using the combustion of a relatively small fuel quantity with additional oxygen, thus the global oxygen balance in the mixture would not change (Esirgen 2014). However, according to Sarisin (2005), this heating method could slightly change the molecular weight of the mixture. The flow temperature would be controlled by the previously developed algorithm similar to Shynkarenko et al. (2019a). The combustion heater used in the current work has the following advantages: low fuel consumption, simple operation, and low maintenance costs.

As in this work, the fuel line was not assembled, its function is only to continue the airflow, as the other pipes, taking into account local pressure losses when the flow passes through the expansion and compression regions, cavities, and other obstacles like sensors, fuel collector, injectors, flame holder, etc.

Combustion Chamber

A cold flow passes around the ramjet combustion chamber elements: the fuel injectors and flame stabilization system towards the nozzle, losing some part of its total energy. The average flow velocity inside the combustion chamber should be low (M < 0.05) to organize efficiently the combustion process, so the pressure losses here are small. The pressure in the combustor should be high enough for the fluid to reach supersonic velocity at the nozzle outlet (Anderson 2016). The operating pressure of the test engine for hot flow tests is 4 bar and for cold flow tests is 2 bar.

Supersonic Nozzle

A supersonic nozzle aims to accelerate the fluid that passes through it continuously. It consists of two parts: the convergent part, where the flow is subsonic, and the divergent part, where the flow is supersonic, as illustrated in Fig. 3.
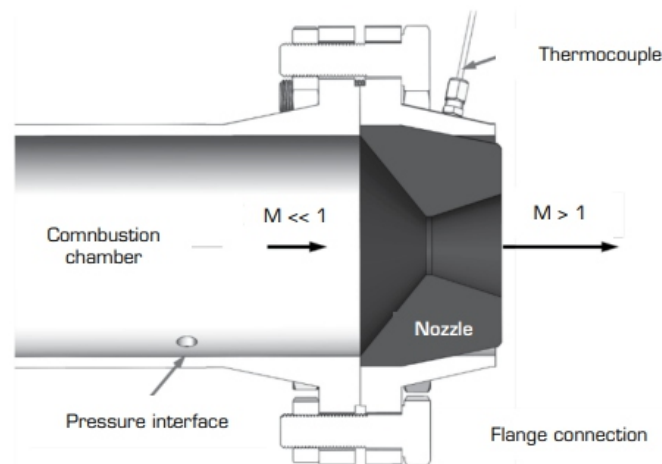
Figure 3. Nozzle subassembly.

Considering that the Mach number M = V/a, where V is the flow velocity and a is the speed of sound, the variation of Mach number along the nozzle can be described by the area-Mach number relation shown in Eq. 1 (Anderson 2016).

$$\left(\frac{A}{A^*}\right) = \frac{1}{M^2}\left[\frac{2}{\gamma+1}\left(1 + \frac{\gamma-1}{2}M^2\right)\right]^{\frac{\gamma+1}{\gamma-1}} \tag{1}$$

where A is any cross-sectional area of the nozzle, A* is the minimum flow area (throat) and ϒ = 1.4 is the air specific heat ratio for the ideal gas. Equation 1 provides two solutions of M for each value of A, one subsonic (M < 1) and one supersonic (M > 1).The graphite nozzle has been used in the current project, material that is characterized by having good thermal shock resistance (Souza 2014) and the melting point between 4000 and 5000 K (Savvatimskiy 2005).

Data Acquisition System

The Data Acquisition System (DAQ) based on the National Instruments CompactDAQ solution has been used in the current research project in order to control the flow system through the electronic devices installed in the engine (control valve positioner and sensors). It is composed by the following modules:

• Chassis NI 9178 has been used as a base module, allowing to send and receive signals from a computer with control software. It also allows to start, pause or stop the data acquisition and to start or pause output signal generation (NI 2016a);

• Current output module NI 9265 has been used to perform generation of the valve control signal of 0–20.6 mA with frequency up to 100 kHz (NI 2015);

• Thermocouple input module NI 9213 has been used to obtain the temperature data in the range of ± 78.125 mV from 16 independent channels, up to 75 S/s (samples per second) per channel (NI 2017);

• Current input module NI 9208 has been used to obtain pressure sensor data, up to 500 S/s per channel from 16 channels. Its input signal amplitude is ± 22 mA, it should be further converted to pressure units using a transformation function (NI 2016b).

Analytical Flow Model

The analytical model of the flow inside the ramjet test engine was calculated from a simplified schematic presented in Fig. 4.

The flow process was considered isentropic in all air duct except the choked flow region on the valve 2. The air expansion in the tank is assumed adiabatic because the engine characteristic operation time is smaller than the characteristic heat transfer time between the gas and the tank wall.
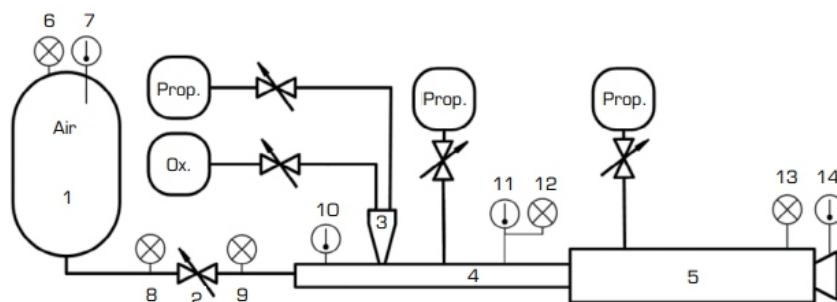
Figure 4. Flow system schematic. 1 – compressed air tank, 2 – flow control valve, 3 – igniter, 4 – airflow heater, 5 – combustion chamber, 6, 8, 9, 12, 13 – pressure sensors, 7, 10, 11, 14 – temperature sensors, Prop. – propellant, Ox. – oxidizer (GOX).

hus, the thermodynamic properties of the flow inside the tank at any time moment could be calculated as described by Eqs. 2 and 3 (Anderson 2003):

$$\frac{p_i}{p_1} = \left(\frac{T_i}{T_1}\right)^{\frac{\gamma}{\gamma-1}} \tag{2}$$

$$p_i V = m_i R T_i \tag{3}$$

where Pi – static pressure at i-th time moment in the air tank; Pi – initial tank pressure at a time t = 0; V – volume of the air tank; mi – mass of air inside the tank; R – specific gas constant, – static temperature in the tank. Local supercritical regime is performed in the section of the control valve 2 (Fig. 4) when the gas velocity becomes supersonic due to the pressure drop on the valve.

The choked flow regime allows to organize aerodynamic and acoustic splitting of the flows between the tank and the engine in such a way that flow perturbations from the engine would not propagate backward in the flow. A normal shock wave equation system has been used in this region, according to Anderson (2016).

The flow in the heater, combustion chamber and nozzle was considered isentropic, following the area-Mach number (Eq. 1).

The supersonic flow in the nozzle exit allows simulating the flight conditions on the test bench because in such cases the ambient conditions would not influence on the chamber pressure. Real-time calculation of the air mass flow rate is based on recorded values of Pi and Ti during the test. The mass flow rate has been numerically calculated; it is based on the experimental mass estimation at every time instance using the following first-order approximation (Eq. 4):

$$\dot{m}_i = \frac{m_i - m_{i-1}}{t_i - t_{i-1}} \tag{4}$$

where m. I – mass flow rate, tI – ti–1 = const – time step.

Due to high thermal inertia in the tank, the airflow temperature measurement would always present a delay caused by a small thermal gradient between expanding gases and the sensor. So, the temperature measurements would be acceptable

only for total conditions, when the temperature is stabilized for a long time, and could also be calculated during the flow process according to Eq. 3.

PID Control Implementation

The control valve and pressure sensors connected to the DAQ form a closed electropneumomechanical system with feedback where pressure after the valve (Fig. 4, it. 9) has been chosen as a goal function. It could be efficiently controlled with the implementation of PID algorithms. The valve opening level has been used as an independent parameter for the mathematical interpretation of a goal pressure function. PID control is generally described as Eq. 5 (Ogata 2010):

$$c(t) = K_p e(t) + \frac{K_p}{T_i} \int_0^t e(t)dt + K_p T_d \frac{de(t)}{dt} \tag{5}$$

Where Kp – proportional gain, Ti – integral time, Td – derivative time, e(t) – "error signal" (the difference between current and desired pressure values), c(t) – controlled value. The input signal could be presented as a step function. The response to this type of function should ideally behave according to Fig. 5 (Ogata 2010).
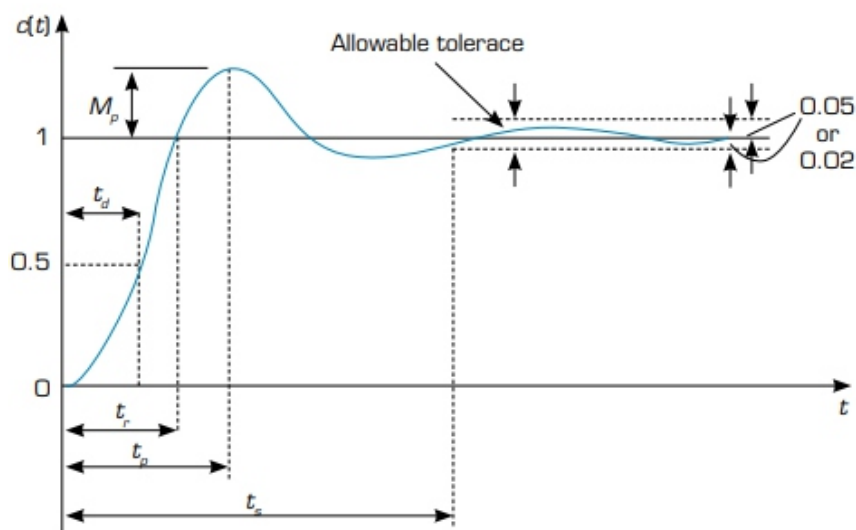
Figure 5. Step function response.

Some characteristics of the output (Fig. 5) could be described as follows:

• Delay time (td) of the response to reach 50% of the final value;

• Rise time (tr) of the response to go from 0 to 100% of the desired value;

• Peak time (tp) to reach the first peak;

• Maximum overshoot (Mp) of the output as a percentage of the final value;

• Settling time (ts) of the process variable to enter and remain within a maximum allowable value range

of 5 or 2% of input error.

A preliminary search of adequate PID characteristics is made using the theoretical methods (Frank 2018). The methods of Ziegler–Nichols and Chien–Hrones–Reswick have been used for the preliminary estimation of the control coefficient values.

Preparation of the Cold Flow Tests

The goal relative pressure of 2 bar on diffuser exit (Fig. 4) was selected for the tests, it corresponds to 17.5 km of flight altitude and M = 3 for a typical ramjet engine, according to Shynkarenko et al. (2019a). Test duration of 20 s has been chosen and the sampling interval tI – ti-1 = 5 ms. In total 4,000 samples have been acquired in each experiment. The air tank initially was pressurized up to 10 bar.

RESULTS AND DISCUSSION

The most relevant data obtained from the cold flow test are illustrated in Figs. 6 to 10. Some data oscillations could be observed on these graphs (noise) due to interference of an electric nature, to which the sensors are subjected, and transient flow processes captured by pressure and temperature sensors. Reduction of the noise has been made applying the filtering process, eliminating high or low frequencies in electric signals (MC 2012) by the DAQ modules.

The maximum pressure error estimated taking into account the sensor characteristics, signal transfer, amplification and transformation function is close to ± 1.0% (Araujo 2019).It is important to emphasize that the pressure sensor measurements are providing more data for the analysis than the thermocouple, due to its slower response time.

In addition, the sampling rate of the thermocouple DAQ module NI 9213 is 75 S/s, it has been interpolated to global data acquisition frequency of 200 S/s by the internal DAQ algorithm. Thus, changes of the flow temperature vary slowly with respect to pressure (Anderson 2016), such a situation does not pose a problem for the analysis of test data.Figure 6 illustrates the variation of the stagnation pressure in the tank and static pressure 8 (Fig. 4) in the line as a function of time.

 The pressure decays as predicted by Eq. 4. The initial tank pressure was near 9.36 bar and the final pressure was close to 7.39 bar. Thus, the pressure drop in the tank during the test was 1.97 bar
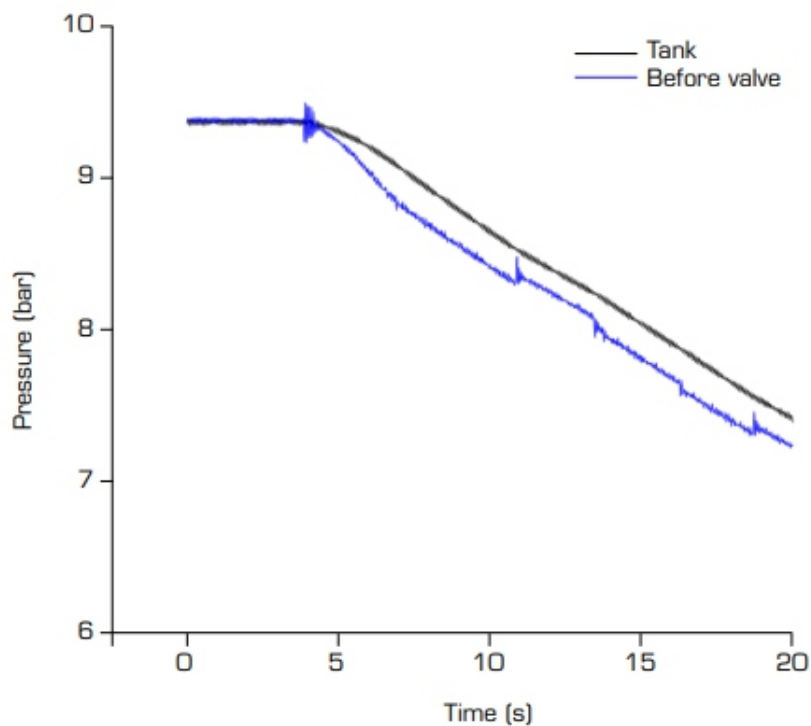
Figure 6. Tank and line pressures in terms of test time.

The pressure before the valve is similar to the tank pressure (Fig. 6). Some small pressure differences could be observed due to the flow movement, compressibility effects ($M \approx 0.1$) and local pressure losses (sudden flow constraint, 4 elbows of 90° and long straight pipes). The pressure drop also depends on the valve opening level, as could be seen in Fig. 6 from 10 to 11 s; more constrained flow results in lower flow velocity and smaller pressure difference. An average pressure drop was found to be around 1.9%. The total pressure drop from the tank to valve characterizes a non-isentropic flow (Anderson 2016) due to bends and inlets (White 2011).

Figure 7 represents the static pressure behavior in the pipe after the valve, controlled by the PID algorithm for two cases: initial and optimized PID values. The initial PID values were found experimentally after a number of tests using the "trial and error" method. Initially predicted by the Ziegler–Nichols method, PID constants were studied on series of experiments. A similarity of the pressure plot with the theoretical curve (Fig. 5) can be noticed. Here, the delay time is 5.04 s, the rise time is 6.25 s, the peak time is 7.45 s, the maximum overshoot is 126%, the final error is 10.49% of the goal pressure. The analysis shows that the system response did not stabilize as the final error was higher than 5%.
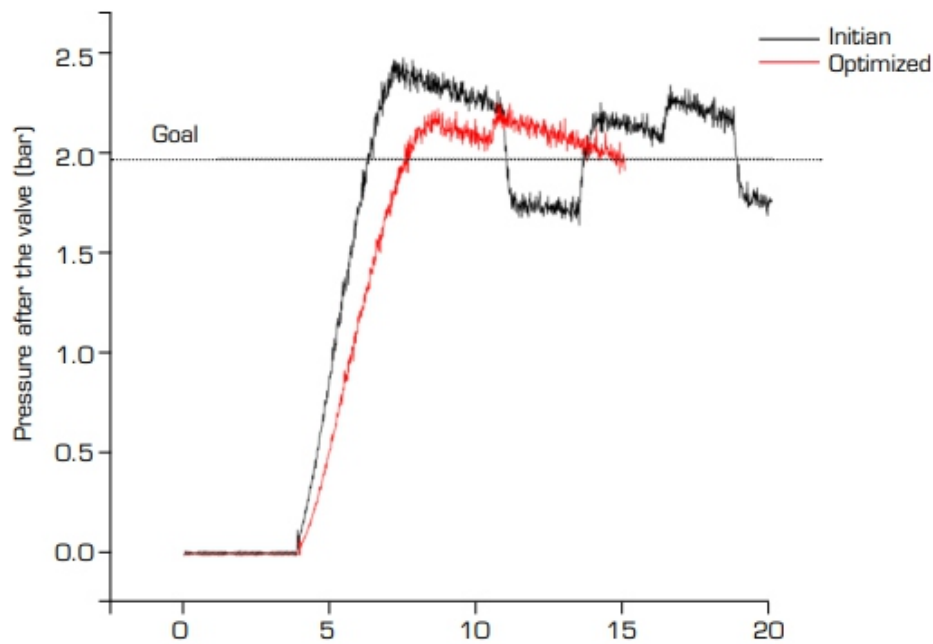
Figure 7. Pressure after the valve (bar) as a function of test time (s).

After experimental identification of PID limits, a large number (hundreds) of experiments have been executed and optimized control constants were found, one of the final results is presented in Fig. 7. It is characterized by 50% reduced overshoot values with respect to the initial pressure variation. Taking into consideration the scale of the test bench and complexity of the experimental setup, optimization of the cold flow control took approximately one year of the experimental work.

The average pressure drop received on the control valve was 6.87 bar, which is consistent with the statement that a commercial valve provides a pressure drop ranging from 5 to 25 bar (Sarisin 2005).

The average pressure drop between the tube after the valve and the heater was 0.018 bar; between the heater and the combustion chamber, an average static pressure increase of 0.008 bar was observed due to the growth of the engine cross-sectional area and flow deceleration.

Figure 8 shows the temperature variation in the tank measured experimentally and estimated numerically by Eq. 3. The measured initial temperature was 24 °C and the final temperature was 21 °C, where the calculated final temperature was 4 °C.
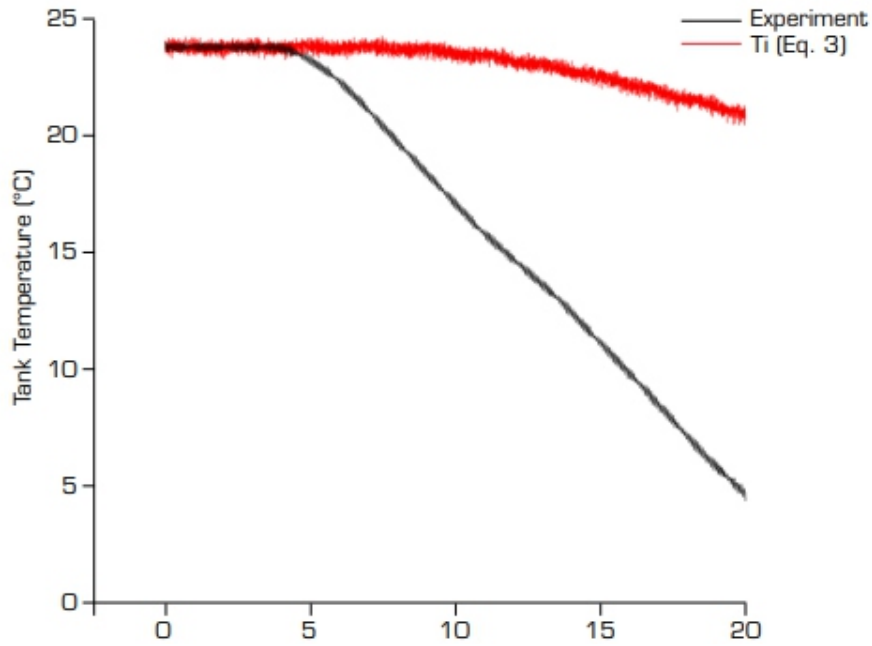
Figure 8. Tank temperature (°C) as a function of test time (s).

Figure 9 shows the air mass flow rate calculated by Eq. 4 based on experimental measurements of pressure in the tank. As a result of processing of the pure experimental data, the noise in the output result (Fig. 9) could be observed. The trendline has been built over the pure result allowing to filter the oscillations and to present the mass flow rate function in a more continuous way. The average mass flow rate of air was 0.55 kg/s, a total air mass consumption during the test was 8.55 kg. Considering that the initial air mass is 55.02 kg, the relative air consumption was around 15.5%.
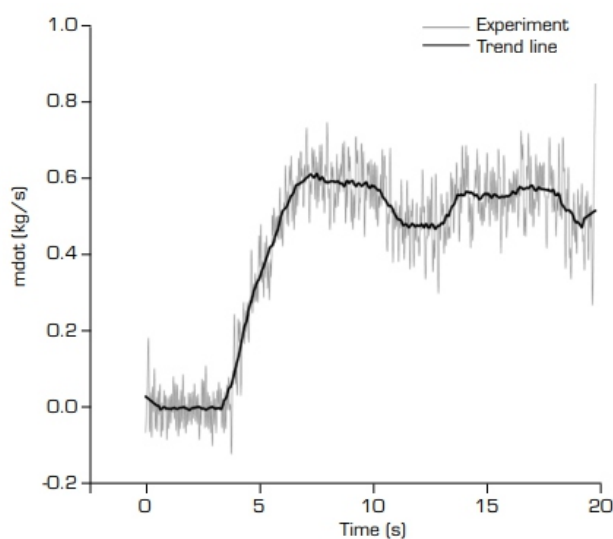
Figure 9. Mass flow rate (kg/s) as a function of test time (s).

Figure 10 shows the variation of the control current applied to the valve positioner during the test for the initial and optimal flow cases. Its initial value of 6 mA corresponds to the fully closed position and 20 mA to fully open position. This plot demonstrates sensitivity of optimal flow control to the input signal, where precise signal output directly influences on the quality of the flow regulation.
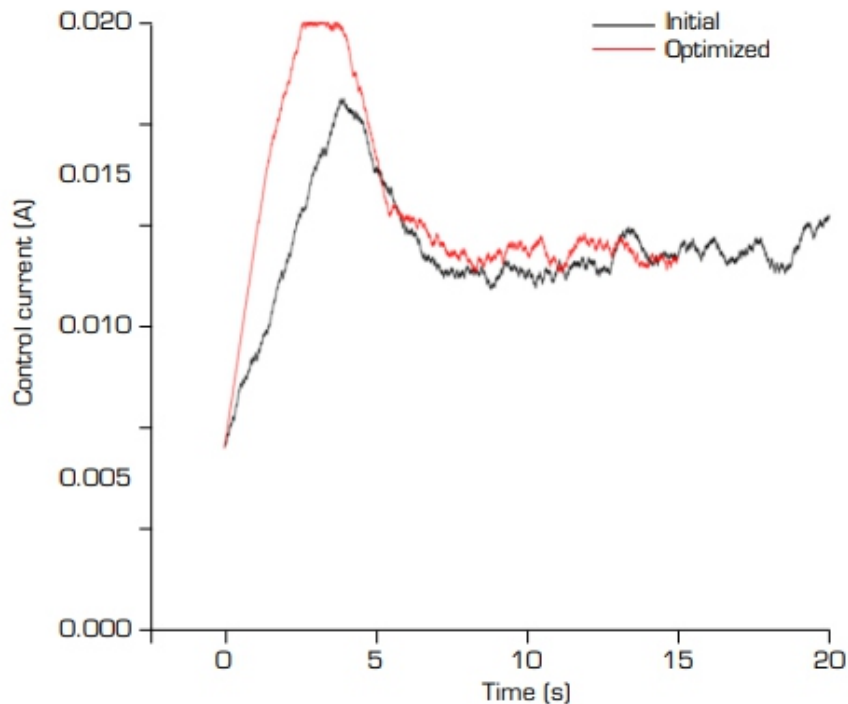
Figure 10. Valve control input (A) as a function of test time (s).

CONCLUSIONS

Theoretical and experimental studies of cold airflow control inside a ramjet engine made possible to estimate and prove the test methodology and to determine the PID control parameters in the system, to link them to the flow parameters measured by temperature and pressure sensors. This study is fundamental for the stable operation of the ramjet engine.

The main results can be summarized as follows:

• The cold gas test system for a ramjet engine was built, assembled and tested;

• The analytical flow model in the air supply system was built and tested experimentally;

• The optimal characteristics of the PID control system were defined as: delay time at 5.04 s, rise time at 6.25 s, peak time at 7.45 s, maximum overshoot in optimal flow test at 110%, final pressure error at 0.23%;

• The optimal PID operation parameters for the test ramjet engine were experimentally found, resulting in a reliable and repeatable airflow system operation, having low overshoot and pressure error.

Current results will allow in the future to perform the experimental study of a hot flow and to prepare the operation tests of the developed engine.

AUTHOR'S CONTRIBUTIONS

DATA AVAILABILITY STATEMENT

All the datasets were generated during the current study.

FUNDING

ACKNOWLEDGMENTS

REFERENCES

[CPL] Chemical Propulsion Laboratory (2017) Design and development of a high-maneuverability supersonic missile with ramjet engine. Brasília: CPL; [accessed Aug 21 2020]. https://sites.google.com/aerospace.unb.br/cpl/projects/ramjet?

[EAS] Emerson Automation Solutions (2017) Control valve handbook. Marshalltown: Fisher Controls International.

[MC] Measurement Computing (2012) Data acquisition handbook. Norton: Measurement Computing.

[NI] National Instruments (2015) NI 9265 Datasheet. Austin: National Instruments. [accessed Jan 23 2020]. http://www.ni.com/pdf/manuals/374067a_02.pdf

[NI] National Instruments (2016a) NI cDAQTM –9171/9174/9178 User Manual: NI CompactDAQ USB 2.0 Chassis. Austin:

National Instruments. [accessed Jan 23 2020]. http://www.ni.com/pdf/manuals/372838e.pdf

[NI] National Instruments (2016b) NI 9208 Datasheet. Austin: National Instruments. [accessed Jan 23 2020]. http://www.ni.com/

[NI] National Instruments (2017) NI 9213 Datasheet. Austin: National Instruments. [accessed Jan 23 2020]. http://www.ni.com/pdf/manuals/374916a_02.pdf

Anderson JD (2003) Modern compressible flow: with historical perspective. New York: McGraw-Hill.

Anderson JD (2016) Fundamentals of aerodynamics. New York: McGraw-Hill.

Araujo WS (2019) Metodologia de aquisição de dados experimentais em propulsão química (BSc thesis). Brasília: Universidade de Brasília. In Portuguese.

Danfoss (2016) Pressure transmitter for general purpose. Type MBS 1700 and MBS 1750. Nordborg: Danfoss; [accessed Oct 29 2020]. https://assets.danfoss.com/documents/DOC354735864202/DOC354735864202.pdf

Esirgen B (2014) Numerical and experimental investigation of direct connected ramjet test facility (Master thesis). Ankara: Middle East Technical University.

Frank SA (2018) Control theory tutorial: basic concepts illustrated by software examples. Cham: Springer. https://doi.org/10.1007/978-3-319-91707-8

Fry RS (2004) A century of ramjet propulsion technology evolution. J Propuls Power 20(1):27-58. https://doi.org/10.2514/1.9178

Hill PG, Peterson CR (1992) Mechanics and thermodynamics of propulsion. Boston: Addison-Wesley.

Inman DJ (2014) Engineering Vibration. New Jersey: Prentice Hall.

Mouritz AP (2012) Introduction to aerospace materials. Sawston: Woodhead Publishing. https://doi.org/10.2514/4.869198Ogata K (2010) Modern control engineering. New Jersey: Prentice Hall.

Omega Engineering (2019) Super OMEGACLAD® XL thermocouple probes: A technological advance in temperature measurement. [accessed Jan 23 2020]. https://br.omega.com/omegaFiles/temperature/pdf/KMTXL_NMTXL.pdf

Sarisin MN (2005) Design of a connected pipe test facility for ramjet applications (Master thesis). Ankara: Middle East Technical University.

Sarisin MN, Tinaztepe HT, Ulas A, Albayrak K (2006) Conceptual design of a connected pipe test facility for ramjet applications.

Paper presented 42nd AIAA/ASME/SAE/ASEE Joint Propulsion Conference & Exhibit. AIAA; Sacramento, California, United States. https://doi.org/10.2514/6.2006-4446

Savvatimskiy AI (2005) Measurements of the melting point of graphite and the properties of liquid carbon (a review for 1963– 2003). Carbon 43(6):1115-1142. https://doi.org/10.1016/j.carbon.2004.12.027.

Shynkarenko O, Azevedo, VA, Veras CAG, Alves IPM (2019a) Experimental investigation of hydrocarbon based fuels in solid fuel ramjet. Paper presented 70th International Astronautical Congress. AIAA; Washington, District of Columbia, United States.

Souza NS (2014) Síntese e estudo das propriedades físicas de grafite ferromagnético fluido nanoestruturado (PhD thesis). São Carlos: Universidade Federal de São Carlos. In Portuguese.

Sutton GP, Biblarz O (2010) Rocket propulsion elements. Hoboken: John Wiley Sons.

White FM (2011) Fluid Mechanics. New York: McGraw-Hill

Preliminary Analysis of Solar Cell Interconnections Welding Parameters Using Design of Experiments for Future Optimization

Graziela Fernanda de Souza Maia1,* , Marcelo Lopes de Oliveira e Souza1 , Alírio Cavalcanti de Brito1

Instituto Nacional de Pesquisas Espaciais – Curso Engenharia e Tecnologia Espaciais - Engenharia e Gerenciamento de Sistemas
Espaciais – São José dos Campos/SP – Brazil.

A B S T R A C T

One of the processes that determine the reliability of solar panels used in space applications is the welding of interconnections between two adjacent solar cells. This process has various technologies, sequences and activities that have various characteristics, factors and parameters. Their combinations and values allow countless possibilities, making their adjustments time consuming, costly and exhausting. One way of abbreviating this, achieving competitiveness and meeting the needs of stakeholders is through the Analysis and Design of Experiments. This technique helps in optimizing the best adjustments to obtain the expected results. Thus, this paper presents a preliminary analysis of the parameters and their interactions of the welding process (by parallel-gap resistance welding) of interconnections between solar cells using design of experiments. In this welding process, the cell undergoes a certain level of degradation. For this reason, it is important to determine which process parameters are important and their proper levels, without big cell degradation. The result of this analysis can be used in the future to optimize the welding process meeting the design requirements for reliability and performance.

Keywords: Parallel-gap resistance welding; Solar cells; Experiment design; Reliability

I. INTRODUCTION

Complex and/or highly integrated systems such as satellites, launchers, airplanes and automobiles are required to assess their reliability throughout their life cycle. Predicting the reliability of equipment used in the space sector has become more elaborate and difficult as these space systems are becoming increasingly complex and/or highly integrated (Santos et al. 2019).

The artificial satellites operate under severe conditions imposed by the space environment and in general or are nonrepaired systems in the space during their operational phase. Among the components of the subsystems that make up the satellite, solar panels suffer the most from the severity of the operating environment, for example space debris, temperature cycling or radiation and others (Baruel 2012).

According to Vaz (1999), solar panels have the function of generating the onboard energy necessary to keep operational all subsystems that integrate the satellite, within the specified consumption ranges during all phases of the mission, the useful life and orbital conditions for which it was designed. The solar panel is composed of solar cells, arranged in columns and rows.

In general, solar cells are the primary generating source of energy for the satellite to be in operation in space. Each of these cells has the function of generating a small amount of electrical energy; therefore, it is up to the project team to determine the number of solar cells required in a solar panel, to supply the necessary energy to the satellite during its useful life (Baruel 2012).

One of the critical processes in the manufacturing of solar panels is the process of welding the interconnectors in the solar cells. The interconnector is the element responsible for conducting the current from one cell to the next and, at the end of a series of solar cells, making the energy available to a terminal or interconnection point (Rauschenbach 1980; Vaz and Vaz 2007).

One of the processes that determine the reliability of solar panels used in space applications is the welding of the interconnections between two adjacent solar cells (Maia et al. 2019). This process has several technologies, sequences and activities that have several characteristics, factors and parameters. The importance and values of these allow for numerous combinations, making their adjustments time-consuming, costly and exhaustive. One way to shorten this, achieve competitiveness and meet the needs of stakeholders is through the Analysis and Design of Experiments. This technique helps in the optimization of the best adjustments to obtain the expected results. Therefore, from the point of view of reliability, one of the main concerns of solar panel manufacturers is the quality of the solder in the interconnections of the cells (Maia et al. 2019).

O'Connor and Kleyner (2012) mention that one of the critical processes for reliability of electronic components is the welding process involved in the manufacturing of these items, as there is a high number of failures attributed to fatigue and cracks that occur in the weld joints.

Thus, one way to obtain increased reliability is through a complete analysis of the process and through the realization of a design of welding experiments. With these two quality tools, it is intended to obtain the optimization of the welding process.

Therefore, this work aims to present an analysis of the welding process (parallel-gap resistance welding) of interconnections between solar cells by analysis and design of experiments.

The experimental data used in this work were obtained through a database of welding process of interconnections in solar cells. With the results of this work, the following benefits can be obtained: (1) to improve and optimize the process involved in the manufacturing of solar panels; (2) provide data about the process to the Product Engineering Group at the National Institute for Space Research (INPE); and (3) increase the performance and service life of solar panels.

BASIC CONCEPTS

This section presents the basic concepts for reading and understanding the article.

Welding Process

The welding process consists in a fabrication technique using two or more metal parts there are joined to form a single piece when one-part fabrication is expensive or unfavorable. During welding process a filler metal may be used or not to facilitate the joining materials. A variety of welding methods exists, including arc and gas welding, as well as brazing and soldering (Callister Junior 2008).

Resistance spot welding (RSW) is an important metal joining process and widely used in sheet metal fabrication. There were lot of applications in the field of, rail coach manufacturing, aerospace and nuclear sectors, electric and electronic industries and automobile industries.

Parallel-gap resistance welding process consists of a pair of electrodes spaced at a predetermined distance that come into contact with the part (for example solar cell interconnector). In this process, the electric current flows through the electrodes and interconnection of the solar cell. The heat generated in the resistance offered by the workpiece raises the temperature of the workpiece to be welded to the welding temperature (melting point or above). The pressure exerted by the electrodes on the workpiece contributes for the joining (Steinmeier 2010; Rauschenbach 1980).

For welding solar cells interconnections, the parallel-gap resistance welding process, presented at Fig. 1, is used. According to Rauschenbach (1980), this is the unique and practical welding process for solar cell interconnections.
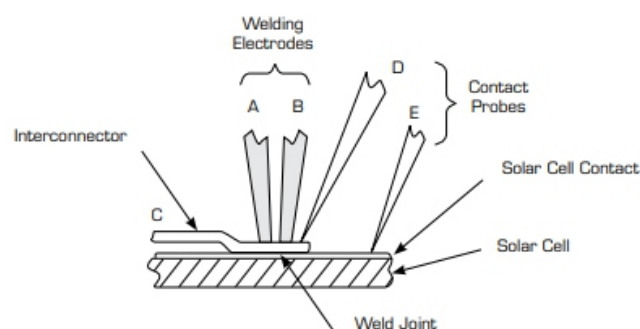
Welding Parameters

The welding parameters (each with a certain value and an appropriate combination between them) establish the conditions that produce the welding process, making possible the joining of the materials. According to Aures (2006), the correct values determine the welding quality.

According to An et al. (2014) and Avila and Bracarense (2017), the main parameters to control and optimize the resistance spot welding are welding current, electrode force and welding time.

The electrical resistance of the part involved in the welding process is extremely important because it is responsible for the Joule effect, but it is not considered a welding parameter (Aures 2006).Table 1 presents the results of literature survey of most significant parameters in an analysis of the spot resistance welding process, using different statistics techniques to analysis these parameters.

Table 1 served as a guide to verify if the chosen parameters were in accordance with industrial and academic practices.

Table 1. Literature survey of parameters and response variable. Source: Maia et al. (2019)

Authors (year)	Parameters considered				Response variable	
Atashparva and Hamedi (2018)	Welding Current	Welding Time	Electrode force	-	Pull test	Height and nugget diameter
Amaral et al. (2018)	Welding Current	Welding Time	Electrode force	-	Pull test	-
Liu (2017)	Welding Current	-	Electrode force	-	Pull test	-
Avila and Bracarense (2017)	Welding Current	Welding Time	-	-	Torsion test	-
Valera et al. (2017)	Welding Current	Welding Time	-	-	Pull test	-
Yue et al. (2016)	Welding Current	Welding Time	Electrode force	-	Pull test	Activation energy
Abrahão et al. (2015)	Welding Current	Welding Time	Electrode force	-	Pull test	-
An et al. (2014)	Welding Current	Welding Time	Electrode force	-	Pull test	-
Souza et al. (2013)	Welding Current	Welding Time	Electrode force	-	Pull test	-
Muhammad et al. (2012)	Welding Current	Welding Time	-	Hold time	Width of HAZ*	Nugget Radius
Maciel Junior (2011)	Welding Current	Welding Time	Electrode force	Time before electrode pressure	Pull test	-
Kim et al. (2007)	Welding Current	Welding Time	Electrode force	-	Indentation	Shear strength

Based on the survey presented in Table 1, the following parameters to be considered for this work will be analyzed: welding voltage, electrode force, welding time and charge involved in the process. The response variable to evaluate the welding joint will be the pull test results.

Welding Current

In this type of welding, both direct current (DC) and alternating current (AC) can be used. In this work, DC was used.

The intensity of the welding current is responsible for the heating of the welded area (Maciel Junior 2011), as the temperature increases, fusion of overlapping materials occurs. This parameter has a suitable value between a minimum and maximum limit that depends on the material of the parts, the thickness, and the contact area between the electrodes and the part to be welded (Santos 2013). According to Santos (2013), a welding current below the minimum limit does not achieve adequate heating and melting in the welded joint region. On the other hand, a current higher than the upper limit causes an unnecessary increase in the heat affected zone (HAZ) by heat, as well as overheating of the weld region, which can lead to plastic deformation of the parts to be welded and excessive electrode penetration with corresponding damage.

Welding Time

Welding time is the duration of welding current distribution to produce the welding point. A very short welding time requires a higher welding current in order to achieve the necessary heat to melt the material (Aures 2006). Short welding time does not melt the material, and it does not produce a good quality welding, which makes the correct control of the welding time critical. In contrast, the longer welding time can expel the liquid, reducing the joint cross section and resulting in a weak and discontinuous weld, as well as overheating the base metal causing it to boil generating gaseous porosity and heat loss through electrodes and parts involved in welding, resulting in defective weld spots (Miller 2010; Carneiro and Barbosa 2015).

Electrode Force

Electrode force has the purpose of press and join the parts that are involved in the welding process, by means of pressure before, during and after supplying the welding current (Aures 2006).

The electrode force on the part should not be excessive because the greater the force, the lower the contact resistance, generating insufficient heat for welding.

An excess pressure of the electrode in the part to be welded can cause the weld fracture, wear of the work pieces due to the penetration of the electrodes, deformation of the electrodes (Dias 2011) and, in the case of solar cells, damage, cracks and breakage because they are fragile components.

Failures in Solar Cells InterconnectionsIn the manufacturing process of solar panels, solar cells are connected to each other by welding the interconnector (in the form of metal strips or wires) into each of the cells, forming the solar modules. The welding process of interconnectors in solar cells is considered a critical step in the manufacture of solar panels (Gierth et al. 2012; Wiese et al. 2010).

One of the considerable threats to the integrity of welded joints is failure due to fatigue. Fatigue establishes crack initiation and propagation and, therefore, the failure of the solder joint.

The most common failure mechanism in welded joints, according to the literature, is caused by cracks that are fundamentally a low-cycle fatigue mechanism, and follows the Coffin-Manson model (Brito 2014).

Thermal cycling in which the materials that make up the solar panel are exposed in space produces expansion and contraction of the materials, causing fatigue and, consequently, failures in the welded joints of the interconnects due to differences in the thermal expansion coefficients of the welded materials (Ferro et al. 1997), this directly affects the reliability of the solar panel during its operational phase. According to Gierth et al. (2012), the main factor contributing to the failures that occur in orbit is due to the thermal expansion that occurs between the solar cell material and the interconnection between them. According to Brennan et al. (1994), the failure of welded joints in solar cell interconnections may compromise or even incapacitate the solar panel to supply power to the satellite or spacecraft subsystems of which they are part.

Design of Experiments

According to Montgomery (2017), design of experiments (DoE) refers to the process of planning the experiments, which were collected and analyzed using statistical methods to provide objective and valid conclusions. The statistical approach to experimental design is necessary when one wishes to draw meaningful conclusions from the obtained data. Figure 2 represents the process as a combination of operations, machines, methods, people, or other resources that turn some inputs into outputs that have one or more observed response variables. Some of the process factors are controllable, while others are uncontrollable or noisy (for example, the interaction between the factors).
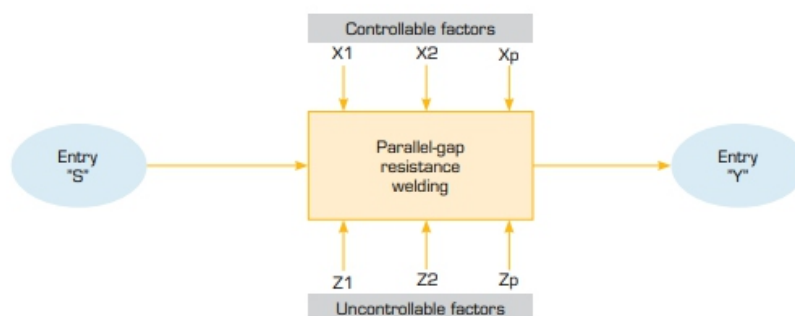
Figure 2. Process to parallel-gap resistance welding. Adapted from: Maia et al. (2019).

Some terms were defined for a better understanding of the design of experiment technique:
Control factors are factors that can be intentionally changed in the experiment in order to evaluate the effects caused on the response variables; and then, allow determining the main factors of the process (Galdámez and Carpinetti 2002).

Response variables are the parameters that suffer some effect in the experiment, when changes are intentionally caused in the factors that control machines in manufacturing processes. In experiments, the variables can be one or more responses that are important to evaluate (Galdámez and Carpinetti 2002).

Uncontrollable factors are factors that cannot be intentionally changed in the experiment, but cause effects on the response variables. For example, interactions between controllable factors, also called noise by some authors; according to Montgomery (2017), it can also be environmental conditions or material properties.

Factor levels are the operating conditions of the process or system control factors. When the tests are carried out, the optimal levels of the control factor or the value closest to that specified by the designers are determined (Galdámez and Carpinetti 2002).

Guidelines for designing of experiments

Figure 3 shows the guidelines applied in design of experiments according to Montgomery (2017). Each step of the guideline is described below.

The first step is the recognition and statement of problem, according to Montgomery (2017), that is to analyze the spot-welding process by electrical resistance used in solar cell interconnections through the technique of analysis and design of experiments.

The selection of the response variable, according to the literature shown in Table 1, as well as the AIAA (2014) standard to assess the influence of input factors in the welding process, is the tensile strength test. However, it is known that there are other means of evaluation; however, with a higher cost and a greater demand for human, financial and infrastructure resources (such as: analysis of the nugget welding by means of ultrasound or microscopy testing, nugget welding sizing etc.).
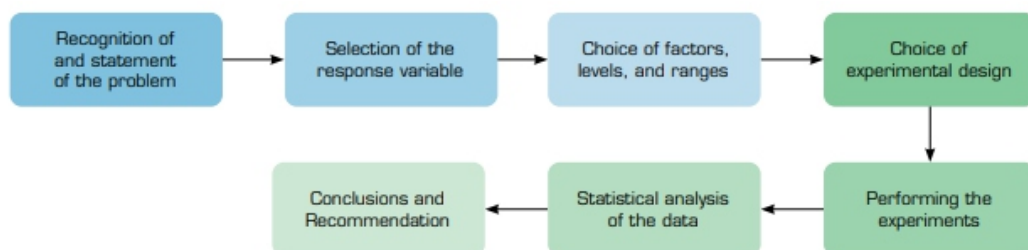
Figure 3. Guidelines for designing of experiments. Montgomery (2017).

Choice of factors, levels, and ranges: the definition of the factors for this work was first carried out by consulting the technical literature (Table 1).

Choice of experimental design. The complete factorial planning, according to Colombari (2004), Souza et al. (2013) and Montgomery (2017), is an experimental technique that consists of carrying out an experiment with k factors, each of these factors being composed of two levels (for example: high and low or lower and higher). It is at this stage that tests are carried out with all possible combinations of preestablished levels of factors.

According to Maciel Junior (2011), the factorial method establishes an optimal model within the levels established for the variables, but there is no guarantee that the specified levels are in the ideal region of operation; therefore, the optimum location may differ from the global optimum. To guarantee a better performance in the process under study, the response surface methodology can be an alternative.

For a better understanding of the complete factorial planning, a statistical model for a factorial experiment 22 is presented in Eq. 1. This can be used as an example for carrying out experiments with as many factors as necessary (Montgomery 2017). However, it is worth mentioning that a large number of factors make the technique unfeasible, since a greater number of experiments is necessary.

$$y = k + k_1 x_1 + k_2 x_2 + k_3 x_1 x_2 \tag{1}$$

where: k is constant; k1 is control factor coefficient x1; x1 is first control factor; k2 is control factor coefficient x2; x2 is second control factor; k3 is coefficient of interaction between factors x1 x2; x1 x2 is interaction between the first and the second control factor.

Experimental matrix. An experiment containing k = 4 factors for a complete factorial is presented in Eq. 2, the calculation performed to determine the number of tests according to the complete factorial technique.

$$2^k = 2^4 = 16 \text{ tests} \tag{2}$$

Table 2 shows a generic experimental matrix, showing 4 factors A, B, C and D, with the combination of minimum and maximum levels. In this table, –1 represents the minimum factor value, and 1 the maximum value.

For this research, the factor A is the electrode force; factor B is welding voltage; factor C is welding time and the factor D is the charge.

According to Souza et al. (2013), the experimental matrix is a way to show all possible combinations of the process parameters and their respective levels.

Table 2. Generic experimental matrix with factors A, B, C and D.

Test. No	Factor A	Factor B	Factor C	Factor D
1	-1	-1	-1	-1
2	1	-1	-1	-1
3	-1	1	-1	-1
4	1	1	-1	-1
5	-1	-1	1	-1
6	1	-1	1	-1
7	-1	1	1	-1
8	1	1	1	-1
9	-1	-1	-1	1
10	1	-1	-1	1
11	-1	1	-1	1
12	1	1	-1	1
13	-1	-1	1	1
14	1	-1	1	1
15	-1	1	1	1
16	1	1	1	1

METHODOLOGY

For this experiment, 36 samples from database was used, that is, four input factors: force of application of the electrode on the part [given in number of steps of the stepper motor]; welding voltage [mV]; welding time [ms]; and charge [in unit of As] were analyzed. The response variable used was the pull test (given in N).

Figure 4 shows the methodology adopted for this work based in guidelines for designing of experiments.
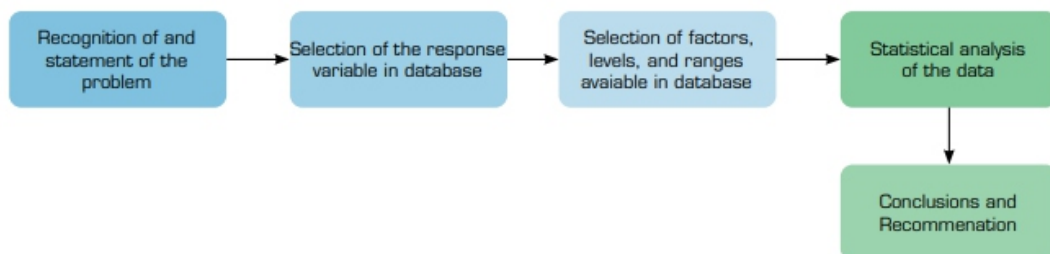
Figure 4. Methodology for this work.

For this work the values of the welding parameters were not revealed in order to preserve the confidentiality of the company's data.Table 3 presents the pull test values for 36 samples. These values were obtained through a device that pulls the sample at 0 degrees in relation to the welded joint, with a speed of 2 mm/min. The pull test values were measured in grams in the device and converted to Newton in the table below.

Table 3. Pull test values for 36 samples.

Test. No	Pull test (N)	Test. No	Pull test (N)	Test. No	Pull test (N)
1	1.5	13	0.9	25	1.4
2	1.5	14	1.1	26	1.6
3	1.4	15	1.4	27	1.5
4	1.4	16	1.7	28	1.5
5	1.2	17	1.5	29	1.5
6	1.4	18	1.9	30	1.8
7	1.4	19	1.9	31	1.8
8	1.4	20	1.8	32	2.6
9	1.6	21	1.5	33	1.5
10	1.2	22	1.4	34	1.5
11	1.3	23	1.4	35	1.5
12	1.1	24	1.2	36	1.6

RESULTS AND DISCUSSION

According to the methodology presented in Fig. 4, the information regarding the welding process was collected in the database and analyzed with the aid of the Minitab 17 software.

The Pareto chart shows the absolute values of the standardized effects from the largest effect to the smallest effect. The standardized effects are t-statistics that test the null hypothesis that the effect is zero. The chart also plots a reference line to indicate which effects are statistically significant.The Pareto chart shows the values of the standardized effects from the highest to the lowest effect.

This plot is represented in Fig. 5, where it is possible to verify the most significant factors for the response variable (pull test). It is possible to verify that the welding time and charge are the most prominent factors; however, they do not exceed the red line that highlights the significant factors.
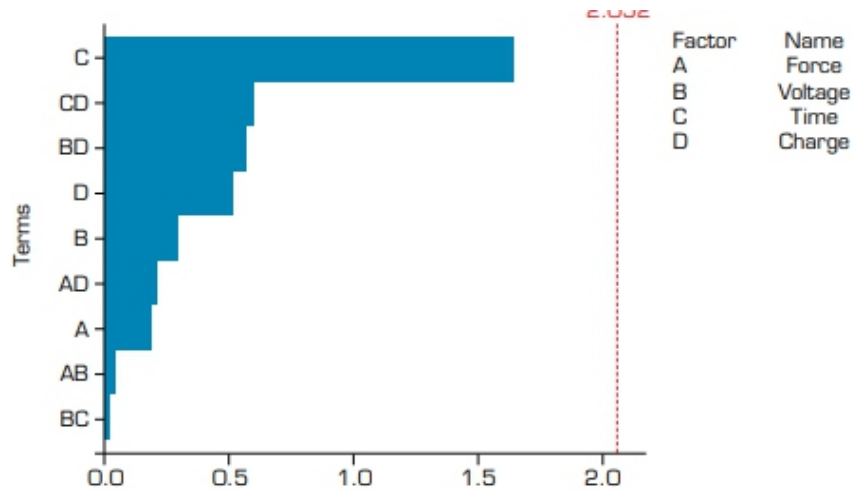
Figure 5. Pareto chart of the standardized effects. Response is Pull Test, α=0.05

In Fig. 5, the parameters that pass the red line are statistically significant at the 0.05 level with the terms of the current model, and the term CD is an interaction of factors C and D as well as BD is an interaction of factors B and D and so on.

If some adjustments are made to the model, the Pareto chart will show only the significant factors, using the regression elimination method, where all factors are included in the initial analysis and then the nonsignificant factors are removed one by one. Applying the method above, it is noted that the effects of factors D (charge) and C (welding time) and the interaction BC (welding time versus voltage) stand out as the most significant factors and interaction, as can be seen in Fig. 6, where the parameters, that pass the red line are statistically significant at the 0.05 level with the terms of the current model.

The third (for example ABC or CDA) and fourth (for example ABCD) order interactions between the factors were disregarded in the Pareto chart in Fig. 6.
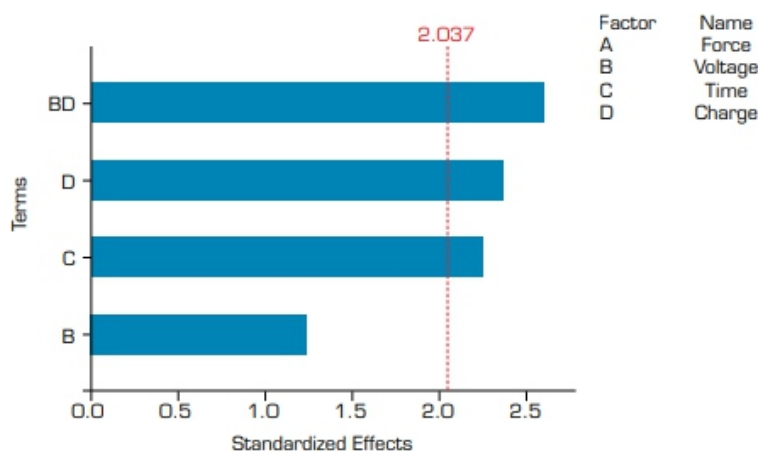
Figure 6. Pareto chart of the standardized effects. (Response is Pull Test, α=0.05)

The main effect plot for pull test as shown in Fig. 7 give the information about the effect of each parameter (factor control) on the response variable (pull test). A main effect is the difference in the mean response between two levels of a factor; the horizontal centerline shows the mean of the pull test for all parameters.
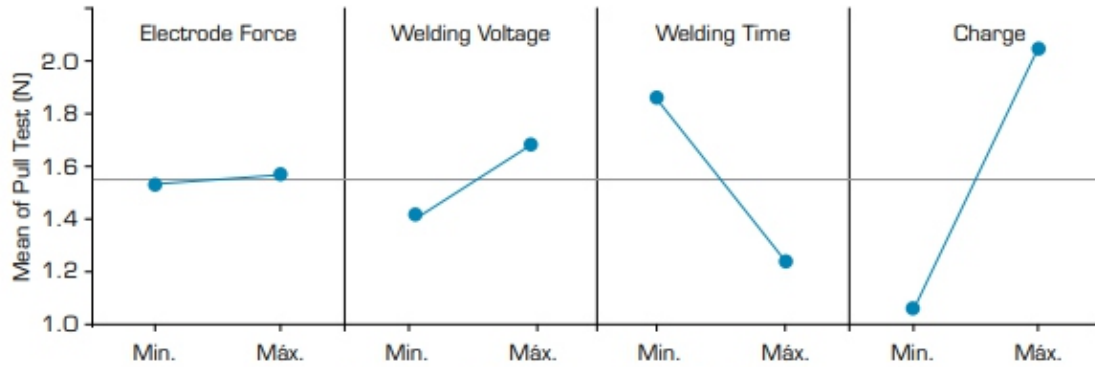
Figure 7. Main effects plot for pull test. Fitted means

The analysis of the plots shown in Fig. 7 is performed based on the variation that the change from the minimum to the maximum level promotes in the response variable; therefore, the greater the variation in the response, the more significant the factor under analysis.

Based on the statement above and on Fig. 7, it appears that charge and welding time are the factors that has the greatest significant effect on pull test. With a higher charge value, a higher pull test value is noted as well as for welding voltage in a smaller scale.

The graphs presented in Fig. 8 show the average of the pull test value versus the interactions between the parameters. In graph when a line is parallel to another, there is no interaction between the factors. When the lines are not parallel, there is a greater strength of the interaction.
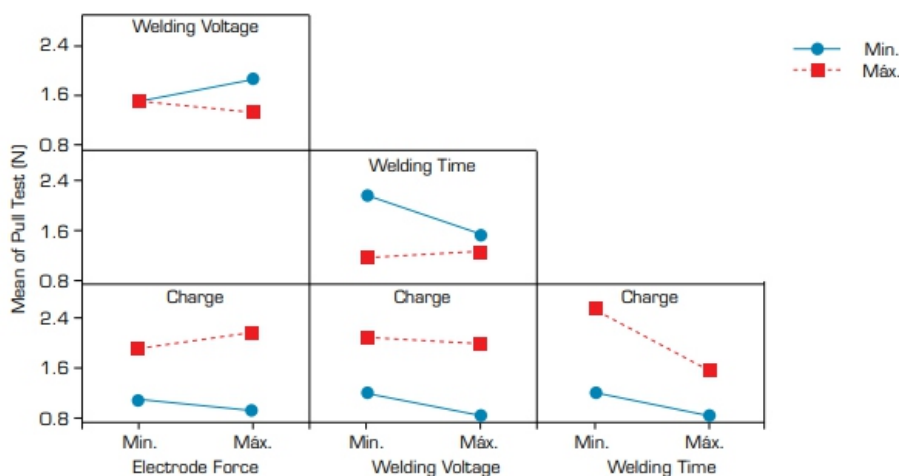
Figure 8. Interaction plot between parameters. Fitted means

For the first graph, there is the interaction between electrode force and welding voltage because the dashed red and blue continuous lines are not parallel. It is observed that when the welding voltage is kept at the minimum value (blue continuous line), the pull test value increases with the increment in the electrode force.

On the other hand, when the welding voltage is kept at maximum value (red dashed line), the pull test value decreases with the increase in the electrode force. It is performed a similar analysis for the other graphs in Fig. 8 for the other factors.CONCLUSIONSAn increase in charge causes an increase in pull test values; on the other hand, with an increase in the welding time, the pull test values tends to decrease, as well as for the welding voltage, however, on a smaller scale.Using the design of the experiment and a database, it was possible to determine, among the four welding parameters, the most important for the process in question; that is, which ones actually had significant effects on pull test.

With the aid of the Minitab 17 statistical analysis software, it was found that the most significant factors in these preliminary tests were the charge, the welding time and welding voltage.

Thus, the experiment design technique proved to be effective in a first analysis of the improvement of the welding process. The methodology was validated as an important tool to be considered when it is intended to reduce costs and the amount of resources to carry out experiments. The use of this tool aims to eliminate defects in manufactured products, in addition to providing a better understanding of the relationship between the factors involved in the process.

It is intended to continue this work aiming at the optimization of the welding process with the use of new based on a planned experimental matrix, in addition to the response surface methodology. For this, additional experiments will be necessary.

AUTHORS' CONTRIBUTION

Conceptualization: Souza MLO; Formal Analysis: Maia GFS; Methodology: Brito AC; Original Draft: Maia GFS; Supervision: Souza MLO and Brito AC.

de Pesquisas Espaciais and to Engenharia Orbital.

REFERENCES

[AIAA] American Institute of Aeronautics and Astronautics (2014) Standard: Qualification and Quality Requirements for Space Solar Cells. Reston: AIAA. https://doi.org/10.2514/4.102806.001

Abrahão ABRM, Reis JF, Brejão SD, Ribeiro VG, Costa ML, Botelho EC (2015) Avaliação dos parâmetros tempo, corrente e pressão na soldagem por resistência elétrica de compósitos PEI/fibras contínuas: influência na resistência mecânica. Matéria 20(2):530-543. https://doi.org/10.1590/S1517-707620150002.0053

Amaral FF, Almeida FA, Costa SC, Leme RC, Paiva AP (2018) Aplicação da Metodologia de Superfície de Resposta para Otimização do Processo de Solda a Ponto no Aço Galvanizado AISI 1006. Soldag Insp. 23(2):129-142. https://doi.org/10.1590/0104-9224/si2302.02

An R, Xu D, Wang C (2014) Parallel-gap resistance welding between gold-plated silver interconnects and silver electrodes in germanium solar cells. Paper presented 15th International Conference on Electronic Packaging Technology. IEEE; Chengdu, China. https://doi.org/10.1109/ICEPT.2014.6922812

Atashparva M, Hamedi M (2018) Investigating mechanical properties of small scale resistance spot welding of a nickel based superalloy through statistical DOE. Exp Tech 42(1):27-43. https://doi.org/10.1007/s40799-017-0221-2

Aures JEV (2006) Estudo da formação, geometria e resistência do ponto na soldagem por resistência: uma abordagem estatística (Master thesis). Brasília: Universidade de Brasília. In Portuguese.

Avila TLD, Bracarense AQ (2017) Influência dos parâmetros de soldagem no ensaio de torção de solda a ponto em um dispositivo automatizado recém desenvolvido. Soldag Insp 22(2):228-237. https://doi.org/10.1590/0104-9224/si2202.11

Baruel MF (2012) Estudo da variação da corrente fotogerada nos painéis solares dos satélites do INPE (Master thesis). São José dos Campos: Instituto Nacional de Pesquisas Espaciais. In Portuguese.

Brennan PC, Jamieson RA, Garcia A, Malachesky PA, Simburger EJ (1994) Evaluation of welded interconnects on thermally cycled silicon solar cells. Paper presented Proceedings of 1994 IEEE 1st World Conference on Photovoltaic Energy Conversion - WCPEC (A Joint Conference of PVSC, PVSEC and PSEC). IEEE; Waikoloa Village, Hawaii, United States. https://doi.org/10.1109/WCPEC.1994.520767

Brito AC (2014) Comparação experimental de técnicas de regressão linear para análise da confiabilidade dos empacotamentos CBGA submetidos à ciclagem térmica e proposta de um novo método para o ajuste e a predição de suas falhas (Doctoral thesis). São José dos Campos: Instituto Nacional de Pesquisas Espaciais. In Portuguese.

Callister Junior WD (2008) Ciência e engenharia dos materiais: Uma introdução. Rio de Janeiro: LTC.

Carneiro MRD, Ba*rbosa RH (2015) Estudo dos parâmetros de solda a ponto com ênfase na soldagem de aços galvanizados.*

Campos dos Goytacazes: Instituto Federal de Educação.

Colombari RR (2004) Aplicação de delineamento de experimentos para o processo de solda à projeção (Master thesis). Itajubá: Universidade Federal de Itajubá. In Portuguese.

Dias JS (2011) Uma metodologia para otimização de parâmetros de soldagem através de solda por resistência aplicada a chapa de aço "Interstitial Free" IF (Master dissertation). Rio de Janeiro: Centro Federal de Educação Tecnológica. In Portuguese.

Ferro RJ, Francis RW, Frasco EB, Pan RB, Pierre-Louis E, Sve C, Berghaus M (1997) Novel techniques for evaluation of interconnections in solar cells used for spacecraft power generation. Paper presented Conference Record of the Twenty Sixth IEEE Photovoltaic Specialists Conference – 1997. IEEE; Anaheim, California, United States. https://doi.org/10.1109/PVSC.1997.654246

Galdámez EVC, Carpinetti LCR (2002) Aplicação das técnicas de planejamento e análise de experimentos no processo de fabricação de produtos plásticos.

Gierth P, Rebenklau L, Michaelis A (2012) Evaluation of soldering processes for high efficiency solar cells. Paper presented 35th International Spring Seminar on Electronics Technology. IEEE; Bad Aussee, Austria. https://doi.org/10.1109/ISSE.2012.6273123

Maciel Junior H (2011) Uso do planejamento e análise de experimentos no desenvolvimento de um processo de solda por resistência elétrica de pequena escala (Master thesis). Itajubá: Universidade Federal de Itajubá. In Portuguese.

Kim T, Park H, Rhee S (2007) Optimization of welding parameters for resistance spot welding of TRIP steel with response surface methodology. Int J Prod Res 43(21):4643-4657. https://doi.org/10.1080/00207540500137365

Liu J (2017) A study on the influence factors of parallel-gap welding heat. Paper presented 18th International Conference on Electronic Packaging Technology (ICEPT). IEEE; Harbin, China. https://doi.org/10.1109/ICEPT.2017.8046625 Maia GFS, Brito AC, Souza MLO (2019) Análise preliminar dos parâmetros e interações do processo de soldagem de interconexões entre células solares empregando projeto de experimentos visando sua futura otimização. Paper presented Anais do 2º Congresso Aeroespacial Brasileiro. CAB; Santa Maria, Rio Grande do Sul, Brazil. https://doi.org/10.29327/2cab2019.224917

Miller (2010) Handbook for resistance spot welding. [accessed May 24 2018]. https://www.millerwelds.com/-/media/millerwelding

Montgomery DC (2017) Design and analysis of experiments. Hoboken: John Wiley & Sons.

Muhammad N, Manurung YHP, Hafidzi M, Abas SK, Tham G, Haruman E (2012) Optimization and modeling of spot elding parameters with simultaneous multiple response consideration using multi-objective Taguchi method and RSM. J

Mech Sci Technol 26(8):2365-2370. https://doi.org/10.1007/s12206-012-0618-x

O'Connor PDT, Kleyner A (2012) Practical reliability engineering. Hoboken: John Wiley & Sons.

Rauschenbach HS (1980) Solar cell array design handbook: The principles and technology of photovoltaic energy conversion. Dordrecht: Springer. https://doi.org/10.1007/978-94-011-7915-7

Santos WA (2013) Estudo da influência dos parâmetros de regulagem na soldagem por resistência na indústria automobilística

(Monography). São Caetano do Sul: Instituto Mauá de Tecnologia. In Portuguese.

Santos CES, Maia GFS, Souza MLO, Rabello APSS (2019) Uma discussão sobre combinar análises da física da falha e até dados de campo a métodos tradicionais para melhorar as predições da confiabilidade de equipamentos eletrônicos. Paper presented Congresso e Mostra Internacionais SAE Brasil de Tecnologia da Mobilidade. São Paulo, São Paulo, Brazil.

Souza MTS, Fernandes MM, Miranda RC (2013) Otimização dos parâmetros de soldagem a ponto por resistência em uma indústria automotiva por meio da análise de experimentos e metodologia de superfície de resposta. Ciência & Engenharia

22(2):131-140. https://doi.org/10.14393/19834071.2013.20995

Steinmeier D (2010) Resistance welding – parallel gap welding basics: micro joining solutions – microTipsTM. Arcadia: CA 91007.

Valera J, Miguel V, Martínez A, Naranjo J, Cañas M (2017) Optimization of electrical parameters in Resistance Spot Welding of dissimilar joints of micro-alloyed steels TRIP sheets. Procedia Manuf 13:291-298. https://doi.org/10.1016/j.promfg.2017.09.074

Vaz CC (1999) Geradores fotovoltaicos: apresentação do curso de tecnologia de satélites (class notes). São José dos Campos: Instituto Nacional de Pesquisas Espaciais. In Portuguese.

Vaz CC, Vaz JV (2007) Manufacturing and testing of the electrical part of solar array for the China-Brazil Earth Resource Satellite – CBERS 2B. Paper presented 19th International Congress of Mechanical Engineering. ABCM; Brasília, Distrito Federal, Brazil.

Wiese S; Meier R, Kraemer F (2010) Mechanical behavior and fatigue of copper ribbons used as solar cell interconnectors. Paper presented 2010 11th International Thermal, Mechanical & Multi-Physics Simulation, and Experiments in Microelectronics and Microsystems (EuroSimE). IEEE; Bordeaux, France. https://doi.org/10.1109/ESIME.2010.5464551

Yue XK, Tong GQ, Chen F, Ma XL, Gao XP (2017) Optimal welding parameters for small-scale resistance spot welding with response surface methodology. Sci Technol Weld Join 22(2):143-149. https://doi.org/10.1080/13621718.2016.120479

Experimental Study of The Insulating Effectiveness of Silicone Rubber Composites by Oxyacetylene Ablation Testing

Artem Andrianov1,* , Jungpyo Lee1 , Gabriela Possa1 , Hiterson de Oliveira Silva1

Universidade de Brasília – Faculdade Gama – Brasília/DF – Brazil

A B S T R A C T

The objective of this study was to characterize the thermal insulation efficiency of the silicone rubber reinforced composites by oxyacetylene torch. These composites reinforced by glass, carbon, ceramics and silica fibers were intended to be used as ablators in a low-thrust hybrid propulsion motor. The back-face temperature measurements were used as a criterion for insulation efficiency of the specimens, whose frontal face is subjected to the oxyacetylene flame for 40 s. The paper includes the results of the ablation rate measurements and the influence of orientation of glass and carbon fibers relatively to the flame direction on the back-face temperature of the specimens.

Keywords: Thermal insulation; Ablation; Oxyacetylene torch; Silicone rubber.

INTRODUCTION

The presented study was motivated by the necessity of a prolonged fire testing of the low thrust hybrid propulsion motor developed at the University of Brasilia (Andrianov et al. 2015). The required operation time of the motor should be at least 40 s, which requires special measures to ensure thermal protection of the motor casing. Thermal protection for hybrids can be adopted from solid propellant rocket motors. In solid propulsion systems, it is performed by internal insulation, which functions as a heat barrier primarily through the mechanism of ablation (Twichell and Keller Junior 1976). Generally, insulators for solid rocket motors are identified by filler (reinforcement) and matrix (binder); the latter identifies the class of insulation material, which can be thermosetting or elastomeric plastic. The most common thermosetting matrix is phenolic resin, a char-yielding material with good temperature resistance (Ahmed 2009), which limits its application for heat insulation of motor casings experiencing high deformations. Thus, body insulations are usually elastomeric composites providing strain tolerance (Youren 1971).

According to an extensive literature review on elastomeric heat-shielding materials for rocketry (Donskoy 1996), the most appropriate elastomeric heat shielding matrices are nitrile-butadiene, ethylene-propylene and silicone organic rubbers.

Fabrication of insulators from the first two elastomers requires a complex technological process including vulcanization at elevated temperatures. Sophisticated manufacturing process may affect the main advantages of a hybrid propulsion technology, such as flexibility and architecture simplicity (Mazetti et al. 2016). At the same time, a wide range of organic silicones does not require complex technological process and can be vulcanized at room temperatures. According to data provided by Donskoy (1996), erosion resistance for silicone elastomer filled with carbon (density 1.16 g/cm3, ablation rate 0.020 mm/s) is slightly greater than for ethylene-propylene rubber filled with asbestos fiber (1.23 g/cm3, 0.015 mm/s), polypropylene rubber filled with carbon (1.24 g/cm3, 0.015 mm/s) and silica (1.45 g/cm3, 0.019 mm/s).

The extensive literature review by Natali et al. (2016) covers all necessary information on types, technology, testing techniques and application of ablative materials in the aerospace industry, including polysiloxanes (or silicones). According to these authors, silicones are effective matrices for thermal protections systems due to: 1) relatively low density 1–1.2 g/cm3; 2) high thermal resistance (owing to high binding energy of silicon-oxygen bond); 3) capability of yielding siliceous/carbonaceous char; 4) high oxidation resistance in comparison to other char yielding polymers. Thermal resistance of silicones is supported by high binding energy of Si-C bond in comparison with C-C bond in the main chain of hydrocarbon elastomers, possibility to rearrange molecular structure under thermal influence and to form cyclic molecular compounds (Donskoy 1996). Polymers with rings in the polymer chain form a high percentage of char during pyrolysis, which improves erosion resistance of insulator (Schmidt 1969). Besides that, a char layer is supported by a silicone backbone structure even in case when a char layer experiences severe conditions of pressure and temperatures up to 1000 °C in the conditions of induced air combustion chamber (Oyumi 1998). More detailed review for thermal degradation mechanism of polysiloxanes is given by Zhou et al. (2006).

It should be noted that high thermal insulation characteristics of silicone elastomers (such as a lower rate of ablation and higher insulation index tested in oxyacetylene flame in comparison to other elastomers: butadiene acrylonitrile, chloroprene, urethane etc.) have been known for a long time (Schmidt 1965).

At some conditions of heating, decomposition of silicone is slower than in phenolic resin (Favaloro 2000): at 700 °C, the volatilized portion for silicone is near 20% and for phenolic resin is near 50%. As the experimental study by Chapman (1966) shows, the ablative material with a silicone resin base produced the highest performance in a moderate range of conditions (heat rate below 1.14 MW/m2 and dynamic pressure below 2.4 kN/m2) provided by electric-arc-heated gas stream in comparison to phenolic and epoxy base materials. Tests with use of small-scale motor burning kerosene-oxygen

showed that silicone is more thermally stable and more preferred polymer matrix than the phenolic resin for ablative components of vertical launch systems subjected to exhaust plume from solid rocket motors (Koo et al. 2011; Miller et al. 1994).

Yang et al. (2013a) showed that the silicone rubber filled with silica and carbon fibers in oxyacetylene flame yields the ablative layer, whose thermo-oxidative stability is better than that of unfilled rubber due to formation of silica, silicon carbide and aromatic carbon, which transforms into inorganic carbon. Ablative properties can be improved by reinforcement of silicone rubber with various inorganic fibers: not only carbon (Kim et al. 2008; 2011), but also silicon carbide (Zhang et al. 2016), silicate ceramic (Yu et al. 2014; Zhou et al. 2015), zirconium carbide (Yang et al. 2013b) and others. However, the authors compare efficiency of reinforced composites with a virgin silicone rubber, and it is not clear how various types of fillers affect the insulating effectiveness of silicone composite.

According to Donskoy (1996), there are few information about rubbers reinforced with fabrics. The experimental data on insulating effectiveness for various types of fillers in silicone matrix and elevated heat fluxes are given by Koo et al. (2011).

The objective of the presented study is to fill the data gap in the range of moderate heat fluxes 0.01–0.1 MW/m2 , which are inherent to low-thrust hybrid propellant motors (Nunes et al. 2017). The back-face temperature measurements are used as a criterion for insulation efficiency of the silicone rubber specimens, whose frontal face is subjected to oxyacetylene flame for 40 s. The specimens were reinforced with four types of widely available fabrics and tapes based on glass, carbon, ceramics and silica fibers. Other objectives of the study are the comparison of the mass ablation rate of silicone composites and evaluation of back-face temperature of the specimens with parallel and perpendicular orientation of glass and carbon fibers relatively to the oxyacetylene flame direction.

MATERIAL AND METHODS

The characteristics of silicone rubber composites reinforced by glass, carbon, ceramic and silica fibers with perpendicular and parallel orientation in relation to flame direction are given in Tables 1 and 2, respectively. The silicone rubber was obtained by mixture of polydimethylsiloxanes with inorganic fillers (delivering conditions) and copper phthalocyanine. Polydimethylsiloxane was used as a matrix due to low cost and simple processing. Ablation characteristics of the silicone rubber in conditions of burning of liquid nitrous oxide and solid paraffin fuel grain (conditions of the low-thrust hybrid propellant rocket motor) are given by Milhomem et al. (2017)

Table 1. Silicone rubber composites with perpendicular orientation of plies in relation to flame direction.

Name	Reinforcement		Specimen	
	Description	Superficial density (g/m²)	Thickness (mm)	Density (g/cm³)
MA	Fiberglass mat 450 (E-glass)	450	6.8	1.56
32U	Unidirectional carbon tape 32U	332	6.5	1.45
BI52	Bidirectional carbon tape BI52	200	6.4	1.46
110	Fiberglass fabric 110 (E-glass)	110	6.6	1.58
200	Fiberglass fabric 200 (E-glass)	200	6.4	1.64
300	Fiberglass fabric 300 (E-glass)	300	6.5	1.72
600	Fiberglass fabric 600 (E-glass)	600	5.9	1.65
TSI	Silica fiber fabric TS1000	1280	6.4	1.70
TCE	Ceramic fiber tape FC1200	1460	7.0	1.54

The specimens were manufactured by manual lay-up technology at room temperatures, then cut to dimensions of 50 ± 1 by 50 ± 1 mm. The thickness of specimens was 6.35 ± 0.41 mm. It was provided by appropriate number of plies in the specimens, whose fibers were oriented perpendicularly to flame direction (hereinafter referred to as perpendicular specimens). At least five replicates of each type of specimen were tested. The thickness of specimens with parallel-to flame orientation of fibers (hereinafter referred to as parallel specimens) was provided by cutting. It is necessary to note that parallel specimens practically did not have flexural rigidity, thus they were additionally reinforced by gluing of metal sheets on the back-face.

Table 2. Silicone rubber composites with parallel orientation of plies in relation to flame direction.

Name	Reinforcement		Specimen	
	Description	Superficial density, g/m²	Thickness, mm	Density, g/cm³
110-II	Fiberglass fabric 110 (E-glass)	110	6.4	1.48
200-II	Fiberglass fabric 200 (E-glass)	200	6.5	1.51
300-II	Fiberglass fabric 300 (E-glass)	300	6.4	1.46
32U-II	Unidirectional carbon tape 32U	332	6.4	1.42
BI52-II	Bidirectional carbon tape BI52	200	6.8	1.35

The methodology described in ASTM standard (ASTM 2008) was used as a reference, but with some alterations to attend the objectives of the study (considering availability of appropriate welding equipment on Brazilian market).

The scheme of the oxyacetylene test-bench is shown in Fig. 1a. The specimen is hold by four screws equipped with silicone separators to diminish the loss of heat. The specimen holder has two positions in vertical direction. The lower position is used for installation of specimen in the holder, coupling of thermocouples in adapters and setting of neutral flame in oxyacetylene torch. For a fire testing, the holder is displaced manually to upper position and the tip of lateral thermocouple passes through the flame determining a starting point of burning time. Since the heat fluxes in low-thrust hybrid propellant motors are moderate (Nunes et al. 2017), the welding torch (whose characteristics are given in Table 3) adopted for the test-bench had been selected on the basis of the relatively low heat flux. The same settings were used for all tests: the length of internal cone of the neutral flame was 9 mm, the distance between front face of specimen and torch tip was 9 mm. In spite of the fact that the test-bench could be equipped with five thermocouples (Fig. 1b), the back-face temperature was measured by three K-type thermocouples Omega KMQXL-062U-6 with response time 0.3 s (diameter 1.6 mm).
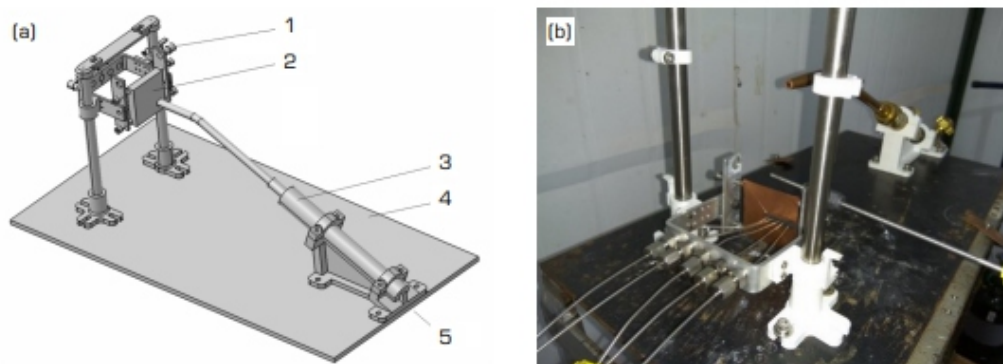
Figure 1. The oxyacetylene test-bench: a) the scheme; 1 – specimen holder; 2 – specimen; 3 – torch; 4 – test-bench plate; 5 – gas hose inlet; b) photograph of the test-bench equipped with five thermocouples for back-face measurements and one lateral thermocouple for timing of burning.

Table 3. Characteristics of welding torch Condor 201 AC#9 adapted for oxyacetylene test-bench.

Pressure (kgF/cm²)		Flow rate (1/h)	
Oxygen	Acetylene	Oxygen	Acetylene
0.10 – 0.40	0.20 – 0.40	220 – 270	210 – 250

The tip of the first thermocouple was installed in the center of specimen's back-face (the central point 0 mm) in such way that the axis of flame would pass through this central point. The tips of the other two thermocouples were displaced along specimen's back-face in lateral direction on distance 4 and 8 mm from the central point. To immobilize the tip of a thermocouple on the back-face of a specimen, the latter was equipped with a silicone rubber strip with five conducting holes spaced 4 mm apart (Fig. 2a). Initial moment of burning time was determined by the thermocouple Omega KMQXL-125U-6 with response time 0.4 s (diameter 3.2 mm), whose tip was installed above the upper edge of a specimen. When the specimen holder dislocates from the lower to an upper position, the thermocouple tip passes through a flame providing an impulse of temperature rise and establishing a starting point. The data from all thermocouples were recorded by data acquisition system Lynx ADS2000.
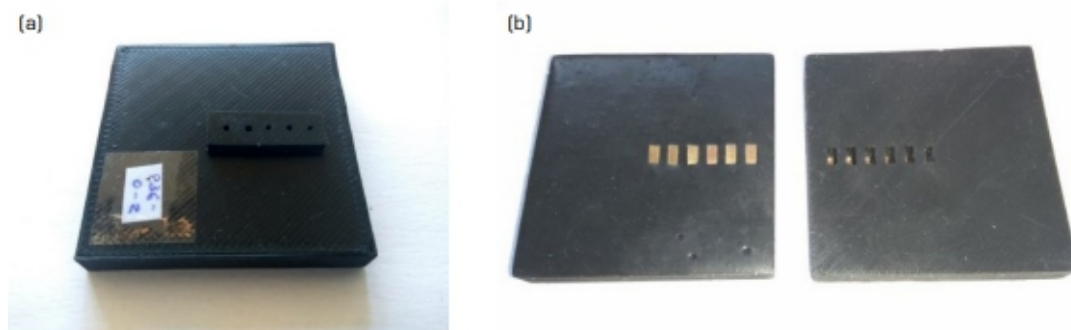
Figure 2. The specimens used in the study: a) the typical specimen of silicone rubber composite; b) the specimen for characterization of oxyacetylene flame (back-face is on the right-hand side).

Since the tested composites were intended to be used as a heat insulator for the low-thrust hybrid propellant motor with operation time no less than 40 s, the same period of time was accepted for the oxyacetylene ablation testing. Mass ablation rate of specimens was calculated by Eq. 1.

$$a = \frac{m_o - m_f}{\delta\tau} \qquad (1)$$

where: mo is the initial mass in g of the specimen; mf is the mass in g of the specimen after burning time $\delta\tau$ (in seconds). A special specimen was prepared for determination of incident heat flux from oxyacetylene heat source. The specimen was made from a material with relatively low thermal conductivity (silicone rubber) and had a shape of a plate with six rectangular through holes spaced 4 mm apart (Fig. 2b). Thin copper sheets with nominal thickness 0.56 mm were embedded into the holes. The specimen front-face was in the same plane as a front surface of the copper sheets, whose back surface was in contact with thermocouple tips.

The temperature measured on the back surface is a result of heat transfer through the thickness of a copper with known thermal properties. The heat transfer through silicone rubber was ignored, because of its low thermal conductivity in comparison with copper and the specimen was exposed to oxyacetylene flame for a short period of time. Heat flux in the first approximation was calculated by the heat diffusion equation (Eq. 2) for the case of unidirectional transfer (Barros et al. 2009):

$$\ddot{q}_x = \rho C_p \delta x \ \frac{\delta T}{\delta \tau} \tag{2}$$

where: ρ is density of copper, kg/m3; C_p is specific heat, J/(kg·K); δx is sheet thickness, m; $\delta \tau$ is the difference between the initial temperature and the temperature after burning period $\delta \tau$ in seconds, K. The maximum burning time $\delta \tau$ for the characterization of incident heat flux was 7 s.

RESULTS AND DISCUSSION

Figure 3a shows one of the five plots of temperature vs time from oxyacetylene flame characterization tests. These data were used for calculation of the heat flux by Eq. 2 for one of the particular coordinates of specimen and burning intervals $\delta \tau$: $0 - 1$ s, $0 - 2$ s, $0 - 3$ s, $0 - 5$ s and $0 - 7$ s (Fig. 3b). Heat transfer from flame to specimen occurs by convection and radiation and depends on temperature of external surface of copper sheets. After observation of data in Fig. 3a, the interval of 2 to 7 s was accepted for calculation of incident heat flux, whose mean values from five measurements are: 114.5 ± 24 kW/m2 for the central point 0 mm, 44 ± 14.5 kW/m2 for the central point 4 mm, 18 ± 4.9 kW/m2 for the central point 8 mm.
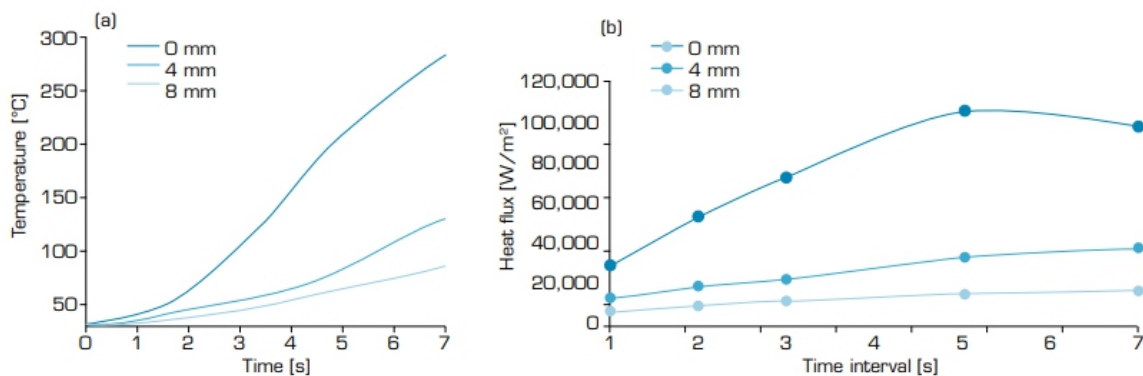
Figure 3. The results of oxyacetylene flame characterization: a) the measured back-face temperature; b) the calculated incident heat flux.

According to the results on insulating effectiveness of the tested specimens reinforced by fibers perpendicularly to direction of oxyacetylene flame (Table 4), the maximum back-face temperature after 40 s is in the range 60–85 °C for all tested specimens. The ranges of temperature for the points 4 and 8 mm are 50–70 °C and 50–65 °C respectively, that indicates practically the same insulating effectiveness of the specimens reinforced by various fibers at the given testing conditions. However, reasons of the similar effectiveness are not the same for all specimens.

Fiber material	Type	Mean thickness (mm)	Temperature after 40 s for three points of measurements (°C)					
			0 mm		4 mm		8 mm	
			Mean	Deviation	Mean	Deviation	Mean	Deviation
E-glass	MA	6.8	58.4	1.3	51.0	2.2	50.1	1.5
	110	6.6	73.4	1.0	58.5	2.3	54.2	2.5
	200	6.4	72.0	3.5	60.7	6.6	50.9	0.3
	300	6.5	66.4	1.9	53.9	3.2	55.0	2.7
	600	5.9	85.8	0.5	70.3	1.8	65.6	4.2
Carbon	32U	6.5	67.5	3.7	61.3	4.3	59.8	6.3
	BI52	6.4	74.4	8.1	65.8	6.6	63.6	7.1
Silica	TSI	7.0	72.9	5.4	62.0	3.0	60.4	2.3
Ceramic	TCE	6.5	79.0	2.3	67.3	4.9	63.9	5.0

It is known that axial thermal conductivity for E-glass fiber is one order less than for a standard-modulus polyacrylonitrile carbon fiber (Zweben 2006). At the same time, the depth of crater in fiberglass specimens is greater than in carbon or ceramic fiber specimens (Fig. 4). The specimens reinforced by glass and carbon fibers (Fig. 4a and 4d, respectively) were subjected to flame for 58 s. As a result, the former specimen has suffered dilatation and the minimal measured thickness through the bottom of the crater was 5.4 mm. At the same time, the latter specimen did not swell and the minimal residual thickness was 6.4 mm. Therefore, for the given testing conditions, lower thermal conductivity of fiberglass specimens is compensated by small residual thickness, and for carbon fiber specimens, higher thermal conductivity is compensated by greater residual thickness
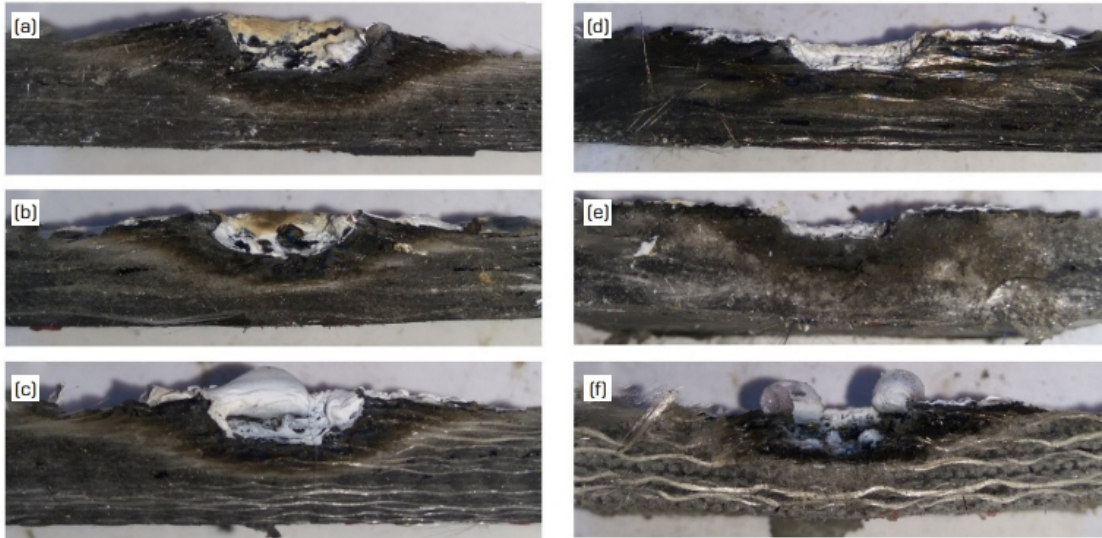
Figure 4. The cross-sections through the center of tested silicone rubber specimens: a) fiberglass 110 (burning time $\Delta\tau = 58$ s); b) fiberglass 600 ($\Delta\tau = 41$ s); c) fiberglass 300 ($\Delta\tau = 41$ s); d) carbon fiber 32U ($\Delta\tau = 58$ s); e) ceramic fiber TCE ($\Delta\tau = 41$ s); f) silica fiber TSI ($\Delta\tau = 41$ s).

It is important to note that ablation rate by mass is lower for fiberglass specimens (Table 5). It can be explained by the effect of full reflection of flame from the front surface of specimen when the crater in specimen takes the semiellipsoid form. In the carbon fiber specimens, such shape of crater does not form (Fig. 4d) and the flame is distributed over the front face of specimen (Fig. 5a). The burning occurs over all front face of specimen and the mass losses are higher. Half of the specimens reinforced with ceramic tape did not have the effect of flame reflection and the shape of crater does not look like profound hemiellipsoid (Fig. 4e). In most of the specimens, the full reflection of flame (Fig. 5c) occurs after some time, which is difficult to determine accurately due to transition effect (Fig. 5b).Figure 6 shows data on temperature measurement on the back-face of specimens, whose fibers have parallel or perpendicular orientation in relation to flame direction. According to the data in Fig. 6, the temperature in the specimens, whose fibers have parallel orientation in relation to flame direction (marked with "-11-"), increases much faster than in specimens with perpendicular orientation of fibers. In the parallel specimens reinforced by fabric, at least half of the fibers is arranged along the thickness of specimen. This portion of fibers serves as a heat conductor, since heat propagates easily along the length of the fibers. As thicker is a fiberglass fabric, as better it conducts a heat in parallel specimens: the temperature on back-face of the specimens 300 is growing faster than on back-face of the specimens 110 and 200 (Fig. 6a). The temperature rises faster in specimens with parallel orientation of carbon fibers than in fiberglass specimens with the same orientation due to higher heat conductivity of carbon (Fig. 6b).For parallel specimens reinforced with carbon fibers, burning time was reduced to 30 s.

In case of burning time above 30 s, these specimens start to deflect due to low flexural rigidity and thermocouples escape from their previous positions. Carbon fibers oriented along the thickness of ablator demonstrate increased resistance to erosion because of high melting temperature of carbon and the roots of the fibers are held by nonheated matrix. After 30 s of burning, there are no sign of thickness reduction in specimens reinforced by carbon fibers in comparison to fiberglass specimens (Fig. 7). High thermal conductivity of carbon is not compensated anymore by greater thickness like in specimens with perpendicular orientation of fibers, therefore the temperature on the back-face of parallel specimens grows faster (Fig. 6a).In perpendicular specimens, there are no fibers oriented along the thickness. The heat from front-face to back-face of specimen propagates through the thickness of fibers and silicone rubber. Since heat conductivity for silicone rubber is lower than for fibers, the temperature growth is slower for specimens with perpendicular orientation of fibers. It explains the least temperature in perpendicular specimen MA reinforced by fiberglass mat (Fig. 6a). Here, fibers are distributed arbitrary in various directions in the plane of ply, which is perpendicular to flame

Table 5. Ablation rates of the tested silicone rubber composites.

Fiber material	Type	Mean thickness, mm	Ablation rate for 40 s, g/s		Full flame reflection time, s	
			Mean	Deviation	Mean	Deviation
Glass	MA	6.8	0.017	0.001	24.9	3.8
	110	6.6	0.017	0.003	28.7	11.2
	200	6.4	0.015	0.002	20.3	4.0
	300	6.5	0.013	0.003	25.1	3.8
	600	5.9	0.015	0.002	28.5	5.9
Carbon	32U	6.5	0.027	0.003	-	-
	BI52	6.4	0.027	0.008	-	-
Silica	TSI	6.4	0.013	0.003	29.2	0.2
Ceramic	TCE	7.0	0.025	0.002	30.3*	0.3*
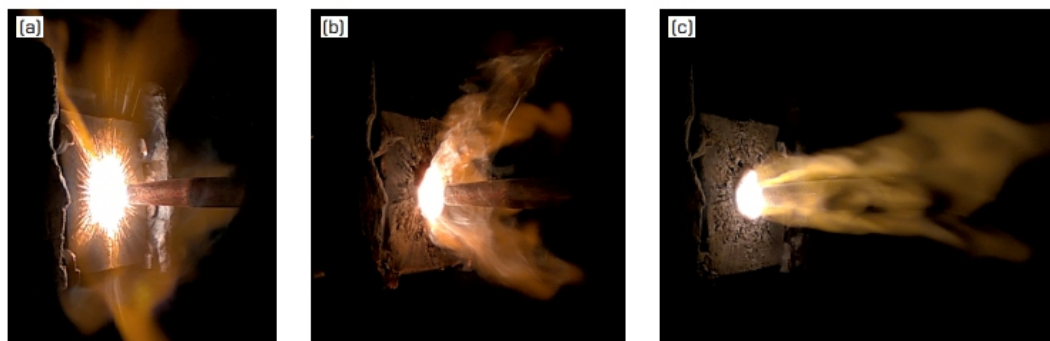
Figure 5. The effect of flame reflection for the same specimen MA: a) no flame reflection; b) partial reflection of flame; c) full reflection of flame.
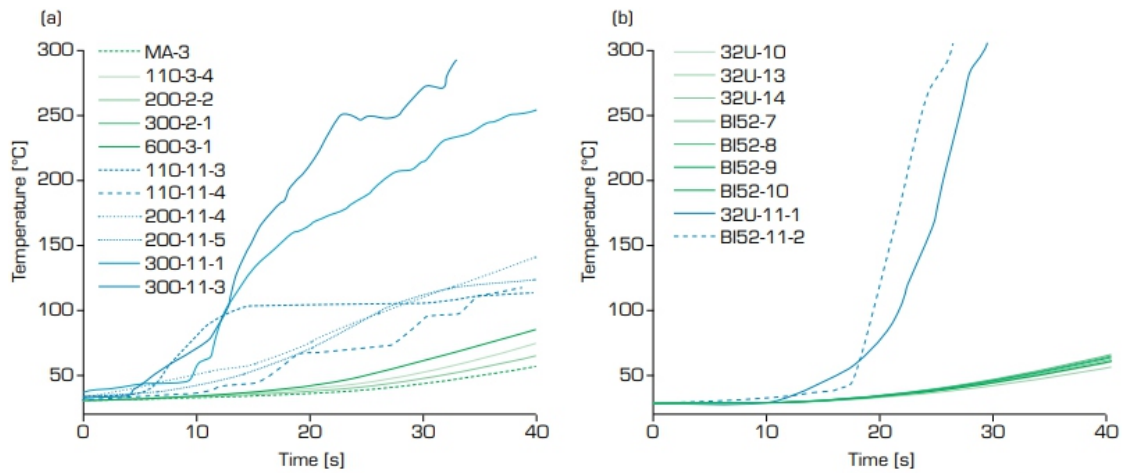
Figure 6. Temperature measurements on back-face central point 0 mm of the selected specimens reinforced by fiberglass (a) and carbon (b) fibers with parallel (blue curves) and perpendicular (green curves) orientation in relation to flame direction.
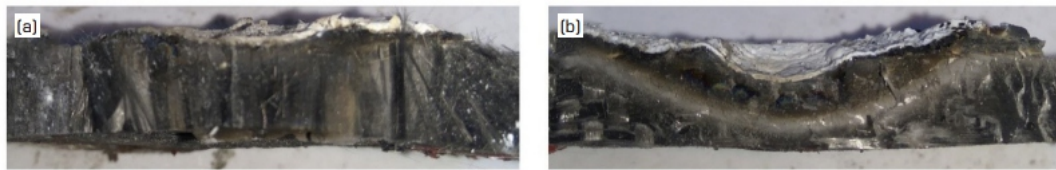
Figure 7. The cross-sections through the center of tested specimens with parallel orientation of fibers in relation to flame direction: a) 32U-11 (burning time $\Delta\tau = 30$ s); b) fiberglass 200-11 ($\Delta\tau = 30$ s).

CONCLUSION

The reinforcement of silicone rubber composites with fiberglass fabric or carbon tape in parallel-to-flame direction is impractical due to low insulating effectiveness. After 40 s of burning, the back-face temperature of perpendicular specimens reinforced by E-glass is in the range 58.4–85.8 °C, while in parallel specimens it exceeds 100 °C. For carbon-reinforced composites, this difference is even greater due to high thermal conductivity of carbon: the back-face temperature of perpendicular specimens is in the range 67.5–74.4 °C after 40 s of burning, whereas in parallel specimens the temperature is greater than 350 °C after 30 s of burning. The comparison of mass ablation rate of parallel specimens was prejudiced by the effect of flame reflection that was observed after 20–30 s of burning in all composites except those reinforced with carbon and ceramic fibers. The latter specimens had higher mass ablation rate 0.025–0.027 g/s than fiberglass and silica specimens, whose mass ablation rate was in the range of 0.013 to 0.017 g/s. For the given conditions of tests (heat flux from the oxyacetylene torch 114.5 ± 24

and burning time 40 s), the tested silicone rubber composites reinforced with E-glass, carbon, silica and ceramic fabrics (or tapes) with perpendicular orientation of plies in relation to the flame direction demonstrated almost the same insulation effectiveness. The least back-face temperature 58.4 ± 1.3 °C was observed in specimens MA reinforced with fiberglass mat (density 1.56 g/cm3); however, the mean thickness of these specimens was slightly higher than in other specimens except those reinforced by ceramic fibers. In spite the fact that the back-face temperature 67.5 ± 3.7 °C in specimens reinforced by carbon tape 32U was higher than in MA specimens, their principal advantage is the least mean density 1.45 g/cm3.It is evident that for low-cost systems, like low-thrust hybrid propulsion rocket motors with relatively short operation time, the less expensive fiberglass composites could be applied for fabrication of internal insulation with insignificant losses in efficiency. However, their efficiency has to be experimentally confirmed in conditions of hybrid propellant rocket motor.

AUTHORS' CONTRIBUTION

Conceptualization: Andrianov A.; Formal Analysis: Andrianov A.; Investigation: Andrianov A., Lee J., Possa G. and Silva H.O.; Methodology: Andrianov A. and Lee J.; Writing – Original Draft: Andrianov A.

DATA AVAILABILITY STATEMENT

All the datasets were generated during the current study.

REFERENCES

Ahmed AF (2009) Thermal insulation by heat resistant polymers (PhD thesis). Montreal: Concordia University. In English.

Andrianov A, Shynkarenko O, Bertoldi AEM, Barcelos Junior MND, Veras CAG (2015) Concept and design of the hybrid test-motor for development of a propulsive decelerator of SARA re-entry capsule. Paper presented 51st AIAA/SAE/ASEE

Joint Propulsion Conference. AIAA; Orlando, Florida, United States. https://doi.org/10.2514/6.2015-3941

ASTM E285-08 (2008) Standard test method for oxyacetylene ablation testing of thermal insulation

Barros EA, Filho GP, Gregori ML, Costa e Silva SF, Charakhovski LI, Maciel HS (2009) *Thermal response and ablation characteristics of quartz-phenolic and carbon-phenolic composites. Paper presented COBEM 2009. International Congress of Mechanical Engineering. COBEM; Gramado, Rio Grande do Sul, Brazil.*

Chapman AJ (1966) *Evaluation of several silicone, phenolic, and epoxy base heat-shield materials at various heat transfer rates and dynamic pressures (technical report). Washington: NASA.*

Donskoy AA (1996) *Elastomeric heat-shielding materials for internal surfaces of missile engines. Inter J Polymeric Mater 31(1-4):215-236. https://doi.org/10.1080/00914039608029377*

Favaloro M (2000) *Ablation materials. In: Kirk-Othmer Encyclopedia of Chemical Technology. Hoboken: John Wiley & Sons. https://doi.org/10.1002/0471238961.0102120106012201.a01*

Kim ES, Kim EJ, Shim JH, Yoon J-S (2008) *Thermal stability and ablation properties of silicone rubber composites. J Appl Polym Sci 110(2):1263-1270. https://doi.org/10.1002/app.28633*

Kim ES, Lee TH, Shin SH, Yoon J-S (2011) *Effect of incorporation of carbon fiber and silicon carbide powder into silicone rubber on the ablation and mechanical properties of the silicone rubber-based ablation material. J Appl Polym Sci 120(2):831-838. https://doi.org/10.1002/app.33139*

Koo JH, Miller MJ, Weispfenning J, Blackmon C (2011) *Silicone polymer composites for thermal protection system: fiber reinforcements and microstructures. J Compos Mater 45(13):1363-1380. https://doi.org/10.1177/0021998310381536*

Mazetti A, Merotto L, Pinarello G (2016) *Paraffin-based hybrid rocket engines applications: A review and a market perspective. Acta Astronaut 126:286-297. https://doi.org/10.1016/j.actaastro.2016.04.036*

Milhomem GP, Nunes APCP, Andrianov A, Shynkarenko O, Lee J (2017) *Experimental studies of heat insulation materials for hybrid propellant rocket motors. Paper presented 24th ABCM International Congress of Mechanical Engineering. ABCM; Curitiba, Paraná, Brazil. https://doi.org/10.26678/ABCM.COBEM2017.COB17-1706*

Miller MJ, Koo JH, Wilson D, Beckley DA (1994) *Effect of reinforcements in a silicone resin composite. Paper presented 32nd Aerospace Sciences Meeting and Exhibit. AIAA; Reno, Nevada, United States. https://doi.org/10.2514/6.1994-787*

Natali M, Kenny JM, Torre L (2016) *Science and technology of polymeric ablative materials for thermal protection systems and propulsion devices: A review. Prog Mater Sci 84:192-275. https://doi.org/10.1016/j.pmatsci.2016.08.003*

Nunes APCP, Milhomem GP, Rispoli VC, Andrianov A (2017) *Application of an inverse method for the estimation of heat flux in low-thrust hybrid propellant rocket motor and its analytical validation. Paper presented XXXVIII Iberian Latin American Congress on Computational Methods in Engineering. CILAMCE; Florianópolis, Santa Catarina, Brazil.*

Oyumi Y (1998) Ablation characteristics of silicone insulation. J Polym Sci A Polym Chem 36(2):233-239. https://doi.org/10.1002/(SICI)1099-0518(19980130)36:2%3C233::AID-POLA4%3E3.0.CO;2-SSchmidt DL (1965) Ablative plastics and elastomers in chemical propulsion environments. Wright-Patterson Air Force Base.

Ohio: Air Force Materials Laboratory, Research and Technology Division, Air Force Systems Command.Schmidt DL (1969) Ablative polymers in aerospace technology. J Macromol Sci – Chem 3(3):327-365. https://doi.org/10.1080/10601326908053818

Twichell SE, Keller Junior RB (1976) Solid rocket motor internal insulation (NASA-SP-8093) (Technical Report). Washington: NASA.

Yang D, Zhang W, Jiang B (2013a) Ceramization and oxidation behaviors of silicone rubber ablative composite under oxyacetylene flame. Ceram Int 39(2):1575-1581. https://doi.org/10.1016/j.ceramint.2012.07.109

Yang D, Zhang W, Jiang B, Guo Y (2013b) Silicone rubber ablative composites improved with zirconium carbide or zirconia. Compos Part A Appl Sci Manuf 44:70-77. https://doi.org/10.1016/j.compositesa.2012.09.002Youren JW (1971) Ablation of elastomeric composites for rocket motor insulation. Composites 2(3):180-184. https://doi.org/10.1016/0010-4361(71)90959-1

Yu L, Zhou S, Zou H, Liang M (2014) Thermal stability and ablation properties study of aluminum silicate ceramic fiber and acicular wollastonite filled silicone rubber composite. J Appl Polym Sci 131(1):39700. https://doi.org/10.1002/app.39700

Zhang G, Wang F, Huang Z, Dai J, Shi M (2016) Improved ablation resistance of silicone rubber composites by introducing montmorillonite and silicon carbide whisker. Materials 9(9):723. https://doi.org/10.3390/ma9090723

Zhou W, Yang H, Guo X, Lu J (2006) Thermal degradation behaviors of some branched and linear polysiloxanes. Polym Degrad Stabil 91(7):1471-1475. https://doi.org/10.1016/j.polymdegradstab.2005.10.005

Zhou C, Yu L, Luo W, Chen Y, Zou H, Liang M (2015) Ablation properties of aluminum silicate ceramic fibers and calcium carbonate filled silicone rubber composites. J Appl Polym Sci 132(11):41619. https://doi.org/10.1002/app.41619

Zweben C (2006) Composite materials. In: Kutz M, editor. Mechanical Engineers' Handbook. Materials and Mechanical Design. Hoboken: John Wiley & Sons. p. 380-417. https://doi.org/10.1002/0471777447.ch1

Space Age: Past, Present and Possible Futures

José Bezerra Pessoa Filho

Departamento de Ciência e Tecnologia Aeroespacial – Instituto de Aeronáutica e Espaço – Divisão de Sistemas Espaciais – São José dos Campos/SP – Brazil.

A B S T R A C T

Since Gagarin's flight on April 12th, 1961, the dream of making human space flight routine and making Homo sapiens a multiplanetary species seemed to have become closer to reality. Nonetheless, on average less than 10 human flights a year have happened along the past 60 years. Unmanned spacecrafts, on the other hand, have changed the way the human race sees itself and the universe it is surrounded by. They have explored all planets in the solar system, as well as comets, asteroids and the Sun. Presently, there are four unmanned spacecrafts on Mars' surface and eight satellites in its orbit. Since the launching of Sputnik in 1957, more than 11,000 satellites have been sent into Earth's orbit. Nowadays, it is impossible to imagine life on Earth without the services provided by the space-based infrastructure resulting from the Space Age. They have changed the modus vivendi of the human civilization and become a commodity, like potable water and electricity. The so-called satellite industry generates around US$ 300 billion a year, mostly related to the sale of satellite services and ground equipment. The era of exponential growth and disruption has reached Earth's orbit, and beyond, through the minds, initiatives and boldness of the NewSpace generation, from which Elon Musk is its exponent. Twenty-five thousand satellites are expected to be launched in the next 10 years to provide, among other applications, worldwide broadband internet access. The scientific community and the military, however, have already expressed their concerns regarding space debris and, as a consequence, space sustainability. For the scientific community, the long-waited launch of the James Webb Space Telescope (JWST) promises to be the 2021 main event. In a time in which Spaceship Earth faces so many challenges, the dream of making its dwellers a multiplanetary species got a revival trough the minds and actions of Elon Musk and Jeff Bezos. There are those who, through public-private partnerships, intend to establish a 1,000 people community working and living in space by 2045. Cooperation among nations has been usual in space, but they are still shy when compared to the efforts required to colonize the Moon, Mars and other places in the solar system. As the 21st century advances, Spaceship Earth faces its greatest challenge ever. Space-based assets provide all the tools required to monitor Earth's health, but if the human species intends to survive as the only identified intelligent civilization, it will have to think and act united in a truly cooperative way. Otherwise, the civilizational and technological effort hitherto undertaken may prove to be useless.

Keywords: Golden Rush; Space Colonization; Space debris; Defense and space; New space; Space 3.0

INTRODUCTION

In April 2021, the 60th anniversary of Yuri Gagarin's historic space flight was celebrated. Less than two months after Gagarin's flight, the USA announced its decision to send humans to the Moon and bring

them back. The impact of Neil Armstrong and Buzz Aldrin's arrival on the Moon, on July 20th, 1969, was such that von Braun predicted that manned flight to Mars would occur in the middle of the 1980s. Indeed, von Braun had always dreamed of a Mars trip (von Braun 1953). Before that, in 1975, the Apollo - Soyuz manned spacecrafts carried out a historic space docking, which for many marked the end of the Cold War in space. In the 1990s, Russia gave up its Mir space station in exchange for its participation in the American initiative to build the International Space Station (ISS), in orbit since 1998. In December 2022, the 50th anniversary of the last manned mission to the Moon will be celebrated, under the expectation that an American woman will land on the Moon by the end of this decade, within National Aeronautics and Space Administration (NASA) Artemis program. Sixty years after Gagarin's flight, sending humans to space is still the exception, not the rule, as less than 600 humans have crossed the border of space, i.e., the 100 km altitude defined as the Kármán line.

In addition to manned flights, the Space Age opened the era of scientific discoveries, the first of which was carried out in 1958 when an experiment aboard Explorer I confirmed the existence of Van Allen belts, named after the scientist responsible for the experiment. Since then, there have been more than 200 unmanned missions to all the planets in the solar system, including the Moon, asteroids, comets and the Sun. So far, the Hubble space telescope has been one of the most outstanding space devices ever, as it registered the birth and death of stars. And what about the more than 4,000 exoplanets discovered in this century, aided by space and terrestrial artifacts(NASA 2021a)? Right now, the lander Insight, the Curiosity and Perseverance rovers and the Ingenuity helicopter, all from NASA, are on the Martian surface looking for signs of life, past or present. Not to forget the six-wheeled Zhurong rover, which made China the second country to ever land a rover on Mars. Around the Red Planet, there are eight artificial satellites, representing the USA, India, Russia, China, United Arab Emirates and the European Space Agency (ESA). In October, an Ariane 5 rocket is scheduled to launch the US$ 10 billion James Webb Space Telescope (JWST), which will be placed near the Earth–Sun L2 Lagrangian point beyond the Moon. The JWST is a joint effort of NASA, the ESA and the Canadian Space Agency (CSA). Besides financial resources and international collaboration, the JWST is a result of a remarkable combination of science, technology and boldness.

From space 1.0 to space 2.0

Part of the achievements presented in the preceding section occurred in the 1950s, 1960s and 1970s, as result of government initiatives, some of which had geopolitical objectives, such as the Apollo Program. Chris Quilty, from Quilty Analytics, qualifies that period as Space 1.0, but, at least in the capitalist world, the governmental resources were invested in private companies. In the Apollo Program, 85% of NASA's resources were spent on 20,000 private companies, involving 360,000 professionals.

In current values, the Apollo Program costs US$ 283 billion(The Planetary Society 2020). In the USA, private companies have always taken part in the space effort. In the past, these companies were hired under "cost-plus" contracts, i.e., they were paid for their expenses plus a profit margin. Nowadays, the private sector is hired under "fixed-price" contracts and, in many cases, it has to share part of the development costs under the expectation it will be rewarded by selling its services to NASA and other interested clients.

Although manned flights have become the most visible part of the Space Age, it was the more than 11,000 satellites launched since Sputnik, in 1957, that changed the modus vivendi of the human civilization. The nearly 3,500 satellites in operation today are part of a space-based infrastructure providing, among others: weather and climate forecasting; communications; data transmission; remote sensing; environmental monitoring; search and rescue; global positioning systems; and object and animal tracking. In 2019, this market generated US$ 271 billion, divided as follows: construction and launching of rockets (2%), construction of satellites (5%), sale of satellite services (45%) and sale of ground equipment (48%)(SIA 2020). On the top of that, governments and commercial human spaceflight have added US$ 95 billion. Countries that are not capable of launching their satellites with their own rockets are deprived of exploring 93% of the market, i.e., sale of satellite services and ground equipment. While inSpace 1.0 the initiatives were all governmental, in Space 2.0 large corporations started to invest in space initiatives, whose genesis can be considered the Iridium constellation, created by Motorola at the end of the 1980s with the goal of providing mobile satellite telephony in remote regions of the globe (Sweeting 2018).

The intra related defense and space worlds

As of December 31st, 2020, there were 3,372 operational satellites in Earth's orbit, belonging, among others, to: USA (1,897), China (410), Russia (176) and India (63) (UCS 2021). These four countries are responsible for 75% of all operational satellites, with the USA accounting for 56% of them. The USA, China, Russia and India occupy the first, second, sixth and seventh positions, respectively, among the countries with the largest investments in space, having already sent unmanned spacecrafts to the Moon and Mars. One aspect that is often overlooked when evaluating the development of the different space programs in the world is their direct relationship with geopolitics and, consequently, with defense. Under the perspective of defense expenditures, the USA, China, India and Russia occupy the first, second, third and fourth positions, respectively. Two hundred and twelve of the 1,897 American satellites have military applications, whereas China, Russia and India have, respectively, 117, 103 and nine military satellites. These four nations have nuclear and anti-satellite (ASAT) weapons. In 2020, the USA spent US$ 738 billion in defense, equivalent to 15% of its federal budget and 40% of the global

defense spending (Gielow 2021). With total revenues of US$ 165.42 billion in 2019, the Americans Lockheed Martin, Boeing, Northrop Grumman, Raytheon and General Dynamics were the five largest arms producing companies in the world. They were followed by Aviation Industry Corporation of China (AVIC), BAE Systems (United Kingdom), China Electronics Technology Group Corporation (CETC), China North Industries Group Corporation (NORINCO) and L3Harris Technologies (USA), with combined revenues of US$ 207.2 billion (Statista 2020). These companies end up working on civilian space projects as well. The importance of space assets in the USA defense is such that in 2019 the United States Space Force (USSF) was created. Its budget for the 2021 fiscal year is US$ 15 billion, two thirds of which to be applied to research, development, test and evaluation (DoD 2021). For comparison purpose, the total cost of Mars2020, the program that took the Perseverance rover to the Martian surface, is US$ 2.7 billion for its 2013–2024 life cycle.

Space 3.0

From a technological point of view, the present century can be defined by the following set of factors: i) internet; ii) miniaturization of electronics, accompanied by increased reliability, processing capacity and decreased costs; iii) smartphones connected to the internet and to satellite global navigation systems; and iv) artificial intelligence. Perhaps who best defined the combined result of this set of factors was Peter Diamandis, coauthor, along with Steven Kotler, of three outstanding books (Diamandis and Kotler 2014, 2015, 2020). Diamandis created the concept "The Six Ds of Exponential Organizations," defined as: digitized, deceptive, disruptive, demonetized, dematerialized and democratized. According to Diamandis (2015)

The 6 Ds are a chain reaction of technological progression, a road map of rapid development that always leads to enormous upheaval and opportunity. (p. 8).

The so-called NewSpace, or Space 3.0, as Chris Quilty prefers, is the result of this exponential technological growth. CubeSats emerged in American universities at the end of last century. CubeSats are defined in terms of U units, which may vary between 0.25 and 27 U, where U represents 10 cm3 modules sizes, with mass bellow 1.33 kg. They are manufactured at low cost with reliable commercial off-the-shelf (COTS) components. The first CubeSats were launched by decommissioned ballistic missiles, or piggyback on commercial rockets, which led to long waiting times. The ISS is also used to launch CubeSats.

What is the use of developing small, cheap satellites if there is no way to launch them at low cost? In 2002, the 30-year-old South African Elon Musk founded a company aimed at building rockets at much lower prices than those offered by the existing providers. So far, SpaceX has flown Falcon 1, Falcon 9 and Falcon Heavy, successfully. It has also, under NASA contracts, launched cargo and humans to the ISS on its Dragon spacecrafts. Falcon 9 recovers and reuses its first stage and fairing, which represent 80% of its total US$ 62 million cost. SpaceX and its 8,000 employees are developing the reusable Starship, the most powerful rocket of all times, with which Musk intends to colonize Mars. Musk's accomplishments have motivated other groups of young entrepreneurs. Founded in 2006 by New Zealand engineer Peter Back, Rocket Lab has developed the remarkable Electron rocket, capable of putting 300 kg into Low Earth Orbit (LEO, bellow 2,000 km of altitude) at a cost of US$ 7.5 million. Electron incorporated innovations in its design, including 3D printing and the use of high-density batteries to power its electro pumps, which feed propellant into the combustion chambers. It has initiated Electron's first stage recovery, together with its nine Rutherford engines and, recently, Peter Back has announced the development of a new and more powerful rocket named Neutron. Rocket Lab has 500 employees and, since 2018, it has launched more than 100 satellites. In 2021 the company is scheduled to launch the Cislunar Autonomous Positioning System Technology Operations and Navigation Experiment (CAPSTONE) CubeSat into lunar orbit, in support to the Artemis Program. On May 15th, however, an Electron rocket experienced a failure, as its second stage single Rutherford engine shut down shortly after ignition. It was Electron's third failure in 20 flights, may be just as a remind that, despite all new technologies, spaceflight is still very hard. It is worth mentioning that NewSpace, or Space 3.0, was brought about not only by advancements in technology, but also by new ways of thinking (things have to be done right, cheaper and safer, at orbital speeds, literally), financing (venture capital) and verticalization (in-house production). Moreover, NewSpace companies are largely personality-driven (Belfiore 2007; Berger 2020; Davenport 2018; Fernholz 2018; Nadis 2020).

The era of exponential growth and disruption has reached Earth's orbit and beyond. Between 2012 and 2019, 3,600 satellites were launched (Bryce Space and Technology 2020), equivalent to one third of all satellites launched since Sputnik in 1957. From those, 70% were SmallSats, i.e., satellites under 600 kg mass, including 1,126 CubeSats. Initially viewed as academic experiments, CubeSats have become reliable commercial platforms. Swarm Technologies uses a constellation of 0.25 U CubeSats, named SpaceBEE, to provide global two-way satellite communications and data relay. Spire Global uses a fleet of 3 U CubeSats, named Lemur, to track airplanes, ships and to provide weather forecast. One of its services is the plotting of efficient ship routes to save on fuel costs. Planet provides 3–5 m resolution images through its 100 3 U CubeSats,named Dove, and 30 other SmallSats. The CubeSat Era reached deep space in 2018, when the 6 U Cubesats, MarCO-A and MarCO-B, flew by Mars and relayed data to

Earth during NASA's Insight entry, descent and landing on the Red Planet.

As technology evolved and satellite size and prices went down, there has been a new surge for the launching of more than 25,000 SmallSats (Pelton and Madry 2020), 90% of them for communications in low Earth orbit (LEO), including the following constellations: Starlink (USA), Kuiper (USA), OneWeb (United Kingdom), Telesat (Canada) and Hongyan (China). The new LEO SmallSat constellations provide a communication delay (latency) one order of magnitude smaller when compared to the 500 communication satellites in geostationary orbit (GEO). This is crucial when one considers that these SmallSats will not only connect people, but billions of devices, including autonomous cars, machines and other services still to be invented, as a result of developments in artificial intelligence (AI), internet of things (IoT) and automated identification services. But these new constellations will face fierce competition coming from 5G communication networks.

Presently, OneWeb constellation is operational with close to 200 SmallSats (150 kg) in LEO. Starlink intends to establish a 12,000 SmallSats (260 kg) constellation in LEO to provide global broadband internet access. So far, over 1,500 Starlink satellites are in orbit and the system is already being tested in some parts of the USA, Canada and Europe. The total estimated cost of Starlink is US$ 10 billion and the constellation is predicted to be fully operational by the end of the decade. If everything goes well, Elon Musk will become the first human being to explore the four segments of the commercial space sector, namely: building and launching rockets; satellite manufacturing (presently, 120 satellites per month); selling of ground equipment (antenna and router); and selling of services (internet access). Today, 45% of the operational satellites in Earth's orbit belongs to Starlink. Besides SpaceX, Musk has also created Tesla, SolarCity, The Boring Company and Neuralink. In 2020, Tesla produced 510,000 cars only, but its market value is superior to Toyota, Volkswagen, Daimler, General Motors, Ford, Honda, Hyundai, Nissan, Renault, BMW and Ferrari combined. His epoch will be marked in history books as BM and AM, meaning before and after Musk, respectively.

Space debris mitigation will be key to the future of space exploration
On January 31st, 2011, there were 975 operational satellites in Earth's orbit. Ten years later, this number has more than tripled, reaching 3,372 satellites (Table 1). A striking feature presented in Table 1 is the increase in the number of satellites operating in LEO. They increased by 464%, whereas the number of monitored orbiting objects increased from 16,102 to 22,079 (CelesTrak 2021). Once the number of satellites in LEO increases by thousands in this decade, the space community concerns on the long-term sustainability of space have also increased. The United Nations Office for Outer Space Affairs (UNOOSA) is the world forum where this important subject is dealt with.

Table 1. Evolution on the numbers of satellites and space debris during the past decade.

Date	Total number of operational satellites[1]	LEO[3]	MEO[4]	GEO[5]	Elliptical orbit[6]	Monitored objects
January 31st, 2011[1]	975	463	63	397	34	16,102[2]
December 31st, 2020[1]	3,372	2,612	139	562	59	22,079[2]

[1](UCS 2021); [2](CelesTrak 2021); [3]LEO – low earth orbit: bellow 2,000 km; [4]MEO – medium earth orbit: between 2,000 and 35,786 km; [5]GEO – geostationary earth orbit: at 35,786 km, on the equatorial plane; [6]Elliptical: eccentricity larger than 1.4 × 10⁻² (Wright 2012).

Defunct satellites, discarded rocket stages, satellite separation subsystems, including small screws, comprise the bulk of space debris. Residual propellant left in the upper stages of satellite launch vehicles may cause their explosion, generating thousands of small pieces. Explosions of overcharged batteries generate space debris as well. It is also possible that defunct satellites break into pieces either by colliding with small space debris or by other unidentified ways. Another source of space debris are anti-satellite weapons (ASAT) tests, as the ones conducted by China and India in 2007 and 2019, respectively. The ESA (2021) estimates, through statistical models, the existence of 900 thousand fragments with sizes varying between 1 and 10 cm, and 128 million pieces between 1 mm and 1 cm.

An eventual collision between a satellite and a piece of space debris generates thousands of smaller pieces which, by their turn, increase the probability of new collisions in a cascade phenomenon known as Kessler effect, in honor of Donald Kessler, a NASA scientist who, in 1978, raised the problem theoretically. Since then, the problem has become real, as demonstrated by the following examples:

• December 1991: A Cosmos-1934 defunct satellite was hit by a piece of debris from a Cosmos-926 satellite, both Russian.
• July 1996: The French military satellite, Cerise, launched in 1995, was hit by a fragment of the Ariane 1 rocket, which exploded 10 years earlier.
• January 2005: An upper stage of an American rocket launched in 1974 was hit by a fragment of a Chinese CZ-4 rocket, whose third stage had exploded in 2000.
• February 2009: An operational Iridium-33 communication satellite collided with Kosmos-2251, a defunct Russian military communications satellite. The collision generated thousands of fragments.
• September 2019: The ESA had to move its Aeolus Earth observation satellite to avoid collision with Starlink-44 satellite (Foust 2019).
• March 2021: The USSF's reported that the American NOAA-17 polar-orbiting weather satellite, decommissioned in 2013, broke into dozens of pieces larger than 10 cm, with no indication it happened as a result of a space debris collision.
• March 2021: The Yunhai 1-02 Chinese meteorological satellite, launched in September 2019, broke into 21 pieces (Foust 2021a).

• April 2021: A close call involving OneWeb-0178 and Starlink-1546 satellites had to be dealt with by maneuvering OneWeb-0178 (Foust 2021b).

• Between 1999 and 2020 the ISS had to be maneuvered 28 times to avoid collision with space debris (Foust 2020).

• May 2021: After launching the first module of the Chinese Space Station, Tianhe, the empty first stage of Long March 5B rocket fell into the Indian Ocean causing concern in the international community (Jones 2021).

Such examples have made some government officials express their concerns publicly. In September 2020, NASA's Administrator Jim Bridenstine tweeted (Foust 2020), as shown in Fig. 1:
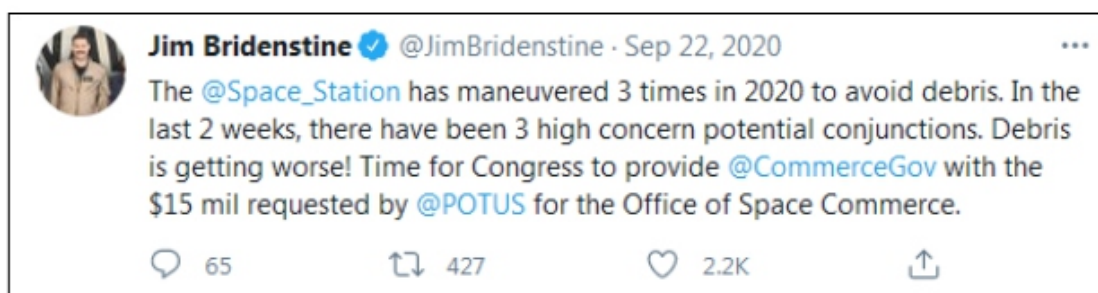
Figure 1. Jim Bridenstine tweet.

As expected, the military have also expressed their concerns. General David Thompson, vice chief of space operations of the USSF said:

Obviously, the Department of Defense wants a voice in that, in terms of what it means to us. We'll have to play our role, whatever it needs to be, but it's definitely time for an agency responsible for regulation and regulatory rules and norms to take a more active role, for both the United States but also in dealing with international bodies. (Erwin 2021)

In a 2021 report, NASA's Office of Inspector General (OIG) stated:

Multiple studies have found that the growth of debris in LEO can be slowed by ensuring that at least 90 percent of all spacecraft are removed from orbit within 25 years of the end of their mission, and at least five defunct spacecraft (that will not deorbit on their own) are actively removed from orbit every year. (NASA 2021b, p. 3)

With regard to the Long March 5B event, the White House press secretary, Jen Psaki, said:

The United States is committed to addressing the risks of growing congestion due to space debris and growing activity in space and we want to work with the international community to promote leadership and responsible space behaviors. (Reuters 2021).

As it becomes clear that mitigation policies will not be sufficient to address the problem, startups and governmental bodies are working on ways of not only monitoring space debris, but also deorbiting them. LeoLabs (2021) uses a network of radars and algorithms to track orbiting objects. Its S-band phased-array radars are capable of tracking 2 cm space debris. ClearSpace, a Swiss based startup, was selected by ESA, among 11 other competitors, to develop a spacecraft capable of using robotic arms to capture space debris. The mission, ClearSpace-1, is scheduled to 2025, when it will try to capture a 100 kg Vega's rocket secondary payload adapter, left in orbit in 2013. After capturing its target object, ClearSpace-1 will deorbit and reenter into Earth's atmosphere, when both will burn up. The ESA is paying ClearSpace € 86 million, which will not cover ClearSpace-1 total development costs. additional funds will come from private investors, who believe to have a business case for future space debris removal (Mathewson 2021).

In March 2021, a Soyuz rocket launched the End-of-Life Services by Astroscale demonstration (ELSA-d) mission (Wade 2021). The payloads are a 17 kg target satellite, which will mock a space debris and a 180 kg chaser satellite. They were launched attached to each other through a magnetic docking plate. Once in orbit, at 500 km, they will execute three different separation and capturing tests, the last of which, to take place later this year, will induce reentry of the chaser-target satellites into the Earth's atmosphere, where they will burn up. The chaser satellite was built by Astroscale, a Japanese startup which got US$ 191 million from private investors. The British Surrey Satellite Technology Ltd (SSTL) was responsible for the target satellite. If everything goes well, Astroscale and SSTL intend to provide capturing and deorbiting services to defunct satellites, which will only work for satellites equipped with their magnetic docking system, as it is the case of the OneWeb constellation satellites (Clark

The "gold rush" in space

The commercialization of space, nonetheless, is not restricted do mega satellite constellations operating in LEO. The Space 3.0 environment contemplates a plethora of bold ideas. One of them, the CisLunar-1000, was presented in 2015 by United Launch Alliance (ULA). It foresees the establishment of a self-sustained space infrastructure capable of keeping 1,000 humans permanently working in space by 2045 (Pyle 2019). By then, according to predictions by ULA, the space economy will reach US$ 2.7 trillion per year. The CisLunar-1000 concept involves the creation of a space ecosystem which includes: the production of rocket propellant; the establishment of orbiting fuel depots; space hotels; solar power satellites (to provide energy to operate in space); water, oxygen and food production; fleets of reusable rockets to allow for the transportation of people and cargo between different locations; robots to produce in situ resources through mining; and fabrication of 3D printed structures using materials available in

space. The idea behind this concept is that it is cheaper to produce in space all needed supplies through in situ resource utilization (ISRU), instead of producing them on Earth and transferring them to space through Earth's steep gravity well. According to Pyle (2019):

The ultimate goal of space infrastructure is the ongoing availability of the assets and resources needed to live and work in space, derived from space-based sources – water and building materials from the moon and asteroids, for example. (p. 205)

Governments will play an important role in establishing the Cislunar-1000 proposal, through public-private partnerships. In 2019, for example, NASA awarded the company Made in Space, a US$ 73.7 million contract to fly the On-Orbit Servicing, Assembly and Manufacturing (OSAM-2) spacecraft, capable of building and assembling complex systems in space through manufacturing. The OSAM-2 is scheduled to be launched no earlier than 2022 by an Electron rocket. Once in orbit, OSAM-2 will 3D print two 10 m beams on each side of the spacecraft. The beams will work as solar arrays. In 2014, Made in Space flew a 3D printer to the ISS, where several components were successfully produced under microgravity conditions. There are also publicprivate initiatives to reduce the cost of sending people and cargo to space. NASA's Commercial Orbital Transportation Services (COTS) allowed for the development of Falcon 9 for US$ 400 million. A study conducted by NASA, using NASA/Air Force Costing Methodology computer modeling, revealed that Falcon 9 would have cost US$ 4 billion if done under traditional NASA practices. Under COTS, NASA did not pay for Falcon 9 total development cost, as SpaceX had to invest its own money under the expectation it will sell Falcon 9 flights to other customers. The same model was successfully used by NASA for hiring SpaceX and Orbital ATK to deliver cargo to the ISS through the Commercial Resupply Services (CRS) Program. In 2014, under its Commercial Crew Program, NASA hired SpaceX and Boeing to develop spacecrafts to ferry astronauts to the ISS. A study conducted by NASA office of inspector general (OIG)revealed that the space agency will pay US$ 90 million/seat to fly astronauts onboard Boeing's CST100 Starliner, as compared to US$ 55 million/seat it pays to fly them onboard Crew Dragon (Wall 2020). As of May 2021, SpaceX has flown three missions to the ISS and Boeing none. NASA is also applying similar procedure to hire the human landing system (HLS) to carry astronauts to and from Moon's surface. SpaceX, Blue Origin and Dynetics are competing for the bid, which now is in the hands of the Government Accountability Office (GAO) and Congress, due to a controversial decision made by NASA, on April 16th, to award US$ 2.89 billion to SpaceX only. It was expected that NASA selected two companies to develop the HLS, but the space agency argued it made the best and cheapest choice given the limited funds provided by the Congress. Blue Origin and Dynetics did not agree with NASA's decision and the bidding process turned into a legal and political

Besides disruptive technologies, management style, internal culture, budget constraints and special interest groups, politics has played an important role on NASA's decision-making process, affecting its accomplishments and costs. Although not related to space directly, Micklethwait and Wooldridge (2020) presented an outstanding discussion on how western governments, the USA and UK included, were not capable of adapting themselves to the disruptive changes which occurred in the past three decades. With regards to the future of human space flight, two lobby groups may be identified, one which defends a direct trip to Mars (Zubrin 2011; 2013) and other which thinks the Moon shall be the next destiny (Spudis 2016). Aldrin and David (2013) suggest the creation of the International Lunar Development Corporation (ILDC) to explore the Moon with rovers operated from Earth. The resulting knowledge would then be applied to Mars, where rovers would be operated by humans from Phobos, one of the two moons of Mars. All groups agree that, next time, the mission should not be to plant a flag only, but to establish human settlements with strategic, scientific and economic purposes. They also think that exploration of the Moon, Mars, asteroids, and even comets will be profitable to the private groups involved. Their rationale is to guarantee the survival of the human civilization against natural (asteroid impact or huge volcanic eruptions) or human made disasters (atomic war or climate change). But since the lifeboat will not be for all, that seems a difficult rationale to sell, as most of the human civilization may end up living in a world as depicted on the 2013 dystopic movie Elysium. Using similar arguments, Elon Musk intends to establish a one million people colony on Mars during his lifetime. Jeff Bezos wants to contribute towards the realization of his childhood dream of establishing human colonies in space, as imagined by his former Princeton professor Gerard O'Neill (1977). The fact that this discussion is led by two billionaires, instead of governmental space agencies, is an indication of how much the space world has changed in the past 20 years, but things are not that simple.

Establishing a Moon outpost is less expensive, risky and difficult than on Mars, where less than half of the 49 unmanned missions were successful. While a one-way trip to the Moon lasts three days on a 400 thousand km journey, it takes 200 days, and more than 400 million km to get to the red planet. The two-way Earth-Moon communication delay is about 3 s, almost "real time" when compared to the 6 to 44 min Earth-Mars-Earth connection time. The longest Apollo mission lasted 12 days, whereas a typical manned Mars mission will take 900 days. The Apollo spacecrafts carried the propellant necessary for the return trip, in addition to food, water and oxygen to breath. In the Martian case, these resources will have to be produced locally by automated machines to be sent in advance, and, if the astronauts are to have a survival chance, they will have to land close to these utilities. That is why SpaceX Starship spacecraft uses methane as fuel, instead hydrogen or kerosene. The idea is to produce methane and oxygen out of the carbon dioxide and water available on Mars. In April, Perseverance MOXIE experiment produced 5 g of oxygen out of the carbon dioxide present in the Martian atmosphere.

It is sufficient to keep a human alive for 10 min. Keeping people in a confined space for one week is one thing, but keeping them confined during a six months one-way journey to Mars is much more challenging. The deleterious psychological and physical conditions of the voyagers upon arrival will limit their ability to operate on Mars. Not to mention the risks imposed to human health by cosmic radiation during the trip itself and on Mars surface. Ten years ago, the Dutch project Mars One (Kraft et al. 2016) tried to simplify the scientific facts and stick with the fiction. Somehow, it mimicked Julio Verne's novel From the Earth to the Moon, published in 1865. Beginning with 4,227 volunteers, Mars One would, after several selection rounds, choose 24 volunteers who would be sent to Mars in six different groups on a one-way trip, at an estimated cost of US$ 6 billion. The Mars One initiative drew a lot of media attention, but in 2019 it was declared bankrupt.Moon's settlement will require hundreds of billion dollars, whereas Mars's settlement will cost many trillions. In a recent interview to Peter Diamandis to announce the US$ 100 million XPRIZE for Carbon Removal (XPRIZE 2021), Elon Musk said "honestly, a bunch of people will probably die in the beginning". Simberg (2014) dedicated a book on the safety issue, which was also dealt with by Zubrin (2013). Their conclusion is: if we are not prepared to face the risks, we would better not even try, as deaths will be certain. At this point, it is worth recalling a cover story brought by The Economist (2011), entitled The end of the Space Age. It stated

Unless life turns up on Mars, or somewhere even more unexpected, public interest in the whole thing is likely to wane. And it is the public that pays for it all.

Therefore, before any decision is made, it will be necessary to develop its rationale and to define who will finance it.The reasoning for the Apollo Program was the Cold War between the USA and the former USSR. In 1970, China became the fifth nation in the world to put a satellite, China 1, into Earth's Orbit. In 2003, it had its first taikonaut in orbit. Four years later the Chinese have placed the spacecraft Chang'e 1 to orbit the Moon, followed by Chang'e2, in 2010. In 2013, China landed Chang'e 3 on the Moon. Since 2015, China overtook Russia in numbers of operational satellites orbiting the Earth. In 2019, Chang'e 4 became the first spacecraft ever to land on the far side of the Moon. In December 2020, Chang'e 5 brought 1.7 kg of lunar rocks back to Earth. On June 23rd, 2020, China completed its global satellite navigation system, Beidou. It was on April 29th, 2021 that a Long March 5B placed the first 22,600 kg module of the Tianhe Chinese Space Station into Earth's orbit. On May 15th 2021, China became the second nation in the world to successfully land a rover on the red planet, Zhurong. In March, China and Russia announced they were developing an International Lunar Research Station (ILRS), comprised of a set of experimental research facilities on and around the Moon. They made it clear that other nations are welcome to join in, but, since 2011 (Wolf Amendment), NASA is forbidden to collaborate with China, unless authorized by the Federal Bureau of Investigation (FBI) and the US

US Congress. Meanwhile, Australia, Canada, Italy, Japan, Luxembourg, New Zealand, South Korea, Ukraine, United Arab Emirates and United Kingdom, have signed Artemis Accords to participate in the American-led program. In this geopolitical competition, India will become an important player, should that country decide to join Russia and China on the ILRS Program. Will that competition open the door for a new space race?

CONCLUSION

In November 1961, Carl Sagan and other 10 scientists got together in Green Bank, West Virginia, USA, to discuss the existence of other intelligent communicative civilizations in the Milky Way galaxy. To direct the discussions, Frank Drake proposed the now famous Drake Equation, composed of seven terms, the last of which related to the amount of time such intelligent civilization would survive before disappearing, either by a natural accident (e.g., asteroid impact) or by its own action (e.g., nuclear war). They concluded there could exist between twenty and fifty million intelligent communicative civilizations, but. sixty years later, no extraterrestrial civilization has shown up.

In December 1968, Apollo 8 astronauts circumnavigated the Moon for the first time. They made the most important discovery of the Space Age ever, synthesized by the astronaut William Anders as shown in Fig. 2:

Figure 2. Earth rise viewed by Apollo 8 astronauts on December 24th 1968.

The Space Age has brought uncountable benefits to the human civilization, but space assets have also provided unquestionable evidence that its development model is not sustainable and a great disruption is under way (Gilding 2011). The World Economic Forum (2021) presented a survey on the global risks perceptions. In terms of probability, extreme weather, climate action failure, human environmental damage, infectious diseases and biodiversity loss occupied the top five positions, whereas in terms of impact infectious diseases, climate action failure, weapons of mass destruction, biodiversity loss and natural resources crises were the top five. The resulting risk matrix left no doubt: if the human race is to survive, it will have to change its competitive mindset to a cooperative one. Impossible? It better not be, as it does not have any better place to go, and time is running out.

REFERENCES

[DoD] Department of Defense (2021) Defense Budget Overview: Irreversible Implementation of the National Defense

Strategy. United States Department of Defense Fiscal Year 2021 Budget Request. Office of the Under Secretary of Defense (Comptroller)/Chief Financial Officer. [accessed May 3 2021]. https://comptroller.defense.gov/Portals/45/Documents/defbudget/fy2021/fy2021_Budget_Request_Overview_Book.pdf

[ESA] The European Space Agency (2021) Satellites vs Debris. ESA. [accessed May 17 2021]. https://www.esa.int/ESA_Multimedia/Images/2021/02/Satellites_vs_Debris

[NASA] National Aeronautics and Space Administration (2021a) Nasa Exoplanet Archive: A Service of NASA Exoplanet Science Institute. [accessed May 3 2021]. https://exoplanetarchive.ipac.caltech.edu/

[NASA] National Aeronautics and Space Administration (2021b) NASA's Efforts to Mitigate the Risks Posed by Orbital Debris [Report n°. IG-21-011]. [accessed May 15 2021].

[SIA] Satellite Industry Association (2020) State of the Satellite Industry Report. [accessed May 3 2021]. https://sia.org/newsresources/state-of-the-satellite-industry-report/

[UCS] Union of Concerned Scientists (2021) Satellite Database: In-depth details on the 3,372 satellites currently orbiting Earth, including their country of origin, purpose, and other operational details. [accessed May 3 2021]. https://www.ucsusa.org/resources/satellite-database

Aldrin B, David L (2013). Mission to Mars: My Vision for Space Exploration. Washington: National Geographic.

Belfiore M (2007) Rocketeers: How a visionary band of business leaders, engineers and pilots is boldly privatizing space. Washington: Smithsonian Books.

Berger E (2021) Liftoff: Elon Musk and the desperate early days that launched SpaceX. Glasgow: William Collins.

Bryce Space and Technology (2020) SmallSats by the Numbers. [accessed May 3 2021]. https://brycetech.com/reports/reportdocuments/Bryce_Smallsats_2020.pdf

CelesTrak (2021) SATCAT Boxscore. [accessed May 16 2021]. https://celestrak.com/satcat/boxscore.phpClark S (2021) Privately-funded mission takes off to begin space debris cleanup trials. Spaceflight Now. [accessed May 17 2021]. https://spaceflightnow.com/2021/03/22/privately-funded-mission-takes-off-to-begin-space-debris-cleanup-trials/

Davenport C (2018) The Space Barons: Elon Musk, Jeff Bezos, and the Quest to Colonize the Cosmos. New York: PublicAffairs.

Diamandis PH, Kotler S (2014) Abundance: The Future Is Better Than You Think. New York: Simon & Schuster.

Diamandis PH, Kotler S (2015) Bold: How to Go Big, Create Wealth and Impact the World. New York: Simon & Schuster.

Diamandis PH, Kotler S (2020) The Future Is Faster Than You Think: How Converging Technologies Are Transforming Business, Industries, and Our Lives. New York: Simon & Schuster.

Erwin S (2021) Space Force sees need for civilian agency to manage congestion. Space News. [accessed May 3 2021]. https://spacenews.com/space-force-sees-need-for-civilian-agency-to-manage-congestion/

Fernholz T (2018) Rocket Billionaires: Elon Musk, Jeff Bezos, and the New Space Race. Boston: Houghton Mifflin Harcourt.

Foust J (2019) Better coordination needed among operators to avoid potential collisions. Space News. [accessed May 3 2021]. https://spacenews.com/better-coordination-needed-among-operators-to-avoid-potential-collisions/

Foust J (2020) Space station maneuvers to avoid debris. Space News. [accessed May 3 2021]. https://spacenews.com/spacestation-maneuvers-to-avoid-debris/

Foust J (2021a) The growing case for active debris removal. The Space Review. Space News. [accessed May 15 2021]. https://

www.thespacereview.com/article/4150/1

Foust J (2021b) SpaceX and OneWeb spar over satellite close approach. Space News. [accessed May 3 2021]. https://spacenews.

com/spacex-and-oneweb-spar-over-satellite-close-approach/

Gielow I (2021) Gasto militar global equivale a 1 ano de Bolsa Família por dia. [accessed May 3 2021]. Folha de S. Paulo. UOL.

https://www1.folha.uol.com.br/mundo/2021/02/gasto-militar-global-equivale-a-um-bolsa-familia-por-dia-em-2020.shtml

Gilding P (2011) The Great Disruption: How the Climate Crisis will Transform the Global Economy. London: Bloomsbury.

Jones A (2021) Long March 5B falls into Indian Ocean after world follows rocket reentry. Space News. [accessed May 17

2021]. https://spacenews.com/long-march-5b-falls-into-indian-ocean-after-world-follows-rocket-reentry/

Kraft N, Kass JR, Kass R, Hooft GT (2016). Mars One, Humanity's Next Great Adventure: Inside the First Human Settlement

on Mars. Dallas: BenBella Books.

LeoLabs (2021): The Mapping Platform for Space. LeoLabs. [accessed May 3 2021]. https://www.leolabs.space/

Mathewson S (2021) ESA partners with startup to launch first debris removal mission in 2025. SPACE.com. [accessed May

17 2021]. https://www.space.com/esa-startup-clearspace-debris-removal-2025

Micklethwait J, Wooldridge A (2020) The Wake-Up Call: Why the pandemic has exposed the weakness of the West - and how

to fix it. London: Short Books.

Nadis F (2020) Star Settlers: The Billionaires, Geniuses, and Crazed Visionaries Out to Conquer the Universe. New York:

Pegasus Books.

O'Neill, GK (1977) The High Frontier: Human Colonies in Space. New York: William Morrow and Company.

Pelton JN, Madry S (2020) Handbook of Small Satellites: Technology, Design, Manufacture,

Pyle R (2019) Space 2.0: How private spaceflight, a resurgent NASA, and international partners are creating a new space age.

Dallas: Ben Bella Books.

Simberg R (2014) Safe is not an option: Overcoming the futile obsession with getting everyone back alive that is killing our

expansion into space. Interglobal Media LLC.

Reuters (2021) U.S. tracking China rocket debris - White House [accessed May 12 2021]. https://www.reuters.com/world/us/

us-tracking-china-rocket-debris-white-house-2021-05-05/

Spudis PD (2016) The Value of the Moon: How to Explore, Live, and Prosper in Space Using the Moon's Resources.

Washington: Smithsonian Books.

Statista (2020) Largest arms-producing and military services companies worldwide in 2019, by arms sales in million U.S

dollars). [accessed May 12 2021]. https://www.statista.com/statistics/267160/sales-of-the-worlds-largest-arms-producingand-military-services-companies/

Sweeting MN (2018) Modern Small Satellites - Changing the Economics of Space. Proc IEEE 106(3):343-361. https://doi.

org/10.1109/JPROC.2018.2806218

The Economist (2011) The end of the Space Age. [accessed May 5 2021]. https://www.economist.com/leaders/2011/06/30/

the-end-of-the-space-age

The Planetary Society (2021) How much did the Apollo program cost? [accessed May 3 2021]. https://www.planetary.org/

space-policy/cost-of-apollo

von Braun W (1953) The Mars Project. Champaign: University of Illinois.

Wade A (2021) Astroscale launches space debris removal mission. The Engineer. [accessed May 15 2021]. https://www.

theengineer.co.uk/astroscale-launches-space-debris-removal-mission/

Wall M (2020) Here's How Much NASA Is Paying Per Seat on SpaceX's Crew Dragon & Boeing's Starliner. [accessed May 3

2021]. https://www.space.com/spacex-boeing-commercial-crew-seat-prices.html

World Economic Forum (2021) The Global Risks Report 2021: Insight Report. [accessed May 3 2021]. http://www3.weforum.

org/docs/WEF_The_Global_Risks_Report_2021.pdf

Wright D (2012) All Things Nuclear: North Korea's Satellite. Union Concerned Scientists. [accessed May 19 2021]. https://

allthingsnuclear.org/dwright/north-koreas-satellite/

XPRIZE (2021) $100M Prize for Carbon Removal. [accessed May 12 2021]. https://www.xprize.org/prizes/elonmusk

Zubrin R (2011) Case for Mars: The Plan to Settle the Red Planet and Why We Must. New York: Free Press.

Zubrin R (2013) Mars Direct: Space Exploration, the Red Planet, and the Human Future. New York: TarcherPerigee

Instructions for Authors

Essentials for Publishing in this Journal

1   Submitted articles should not have been previously published or be currently under consideration for publication elsewhere.

2   Conference papers may only be submitted if the paper has been completely re-written (taken to mean more than 50%) and the author has cleared any necessary permission with the copyright owner if it has been previously copyrighted.

3   All our articles are refereed through a double-blind process.

4   All authors must declare they have read and agreed to the content of the submitted article and must sign a declaration correspond to the originality of the article.

Submission Process

All articles for this journal must be submitted using our online submissions system. http://enrichedpub.com/ . Please use the Submit Your Article link in the Author Service area.

Manuscript Guidelines

The instructions to authors about the article preparation for publication in the Manuscripts are submitted online, through the e-Ur (Electronic editing) system, developed by **Enriched Publications Pvt. Ltd**. The article should contain the abstract with keywords, introduction, body, conclusion, references and the summary in English language (without heading and subheading enumeration). The article length should not exceed 16 pages of A4 paper format.

Title

The title should be informative. It is in both Journal's and author's best interest to use terms suitable. For indexing and word search. If there are no such terms in the title, the author is strongly advised to add a subtitle. The title should be given in English as well. The titles precede the abstract and the summary in an appropriate language.

Letterhead Title

The letterhead title is given at a top of each page for easier identification of article copies in an Electronic form in particular. It contains the author's surname and first name initial .article title, journal title and collation (year, volume, and issue, first and last page). The journal and article titles can be given in a shortened form.

Author's Name

Full name(s) of author(s) should be used. It is advisable to give the middle initial. Names are given in their original form.

Contact Details

The postal address or the e-mail address of the author (usually of the first one if there are more Authors) is given in the footnote at the bottom of the first page.

Type of Articles

Classification of articles is a duty of the editorial staff and is of special importance. Referees and the members of the editorial staff, or section editors, can propose a category, but the editor-in-chief has the sole responsibility for their classification. Journal articles are classified as follows:

Scientific articles:

1. Original scientific paper (giving the previously unpublished results of the author's own research based on management methods).

2. Survey paper (giving an original, detailed and critical view of a research problem or an area to which the author has made a contribution visible through his self-citation);

3. Short or preliminary communication (original management paper of full format but of a smaller extent or of a preliminary character);

4. Scientific critique or forum (discussion on a particular scientific topic, based exclusively on management argumentation) and commentaries. Exceptionally, in particular areas, a scientific paper in the Journal can be in a form of a monograph or a critical edition of scientific data (historical, archival, lexicographic, bibliographic, data survey, etc.) which were unknown or hardly accessible for scientific research.

Professional articles:

1. Professional paper (contribution offering experience useful for improvement of professional practice but not necessarily based on scientific methods);

2. Informative contribution (editorial, commentary, etc.);

3. Review (of a book, software, case study, scientific event, etc.)

Language

The article should be in English. The grammar and style of the article should be of good quality. The systematized text should be without abbreviations (except standard ones). All measurements must be in SI units. The sequence of formulae is denoted in Arabic numerals in parentheses on the right-hand side.

Abstract and Summary

An abstract is a concise informative presentation of the article content for fast and accurate Evaluation of its relevance. It is both in the Editorial Office's and the author's best interest for an abstract to contain terms often used for indexing and article search. The abstract describes the purpose of the study and the methods, outlines the findings and state the conclusions. A 100- to 250-Word abstract should be placed between the title and the keywords with the body text to follow. Besides an abstract are advised to have a summary in English, at the end of the article, after the Reference list. The summary should be structured and long up to 1/10 of the article length (it is more extensive than the abstract).

Keywords

Keywords are terms or phrases showing adequately the article content for indexing and search purposes. They should be allocated heaving in mind widely accepted international sources (index, dictionary or thesaurus), such as the Web of Science keyword list for science in general. The higher their usage frequency is the better. Up to 10 keywords immediately follow the abstract and the summary, in respective languages.

Acknowledgements

The name and the number of the project or programmed within which the article was realized is given in a separate note at the bottom of the first page together with the name of the institution which financially supported the project or programmed.

Tables and Illustrations

All the captions should be in the original language as well as in English, together with the texts in illustrations if possible. Tables are typed in the same style as the text and are denoted by numerals at the top. Photographs and drawings, placed appropriately in the text, should be clear, precise and suitable for reproduction. Drawings should be created in Word or Corel.

Citation in the Text

Citation in the text must be uniform. When citing references in the text, use the reference number set in square brackets from the Reference list at the end of the article.

Footnotes

Footnotes are given at the bottom of the page with the text they refer to. They can contain less relevant details, additional explanations or used sources (e.g. scientific material, manuals). They cannot replace the cited literature.

The article should be accompanied with a cover letter with the information about the author(s): surname, middle initial, first name, and citizen personal number, rank, title, e-mail address, and affiliation address, home address including municipality, phone number in the office and at home (or a mobile phone number). The cover letter should state the type of the article and tell which illustrations are original and which are not.